overactivation of microglia (Akiyama et al., 2000; Gao et al., 2003; Liu and Hong, 2003). Therefore, the regulation of microglia cell activation should be very important issues in the treatment of such diseases. On the other hand, increasing evidence suggests that microglia also play a pivotal role in neuroprotection and that TNF itself is a neurotrophic mediator (Cheng et al., 1994; Gary et al., 1998; Nakajima and Kohsaka, 2004). In fact, we previously demonstrated that microglia that are activated via $P2X_7$ receptors secrete TNF, which in turn rescues the neurons from glutamate-induced cell death (Suzuki et al., 2004). The amounts of TNF released by LPS-stimulated microglia are much higher than the levels that occur from ATP or BzATP-stimulated microglia. Thus, the quantity of TNF released may reflect the state of the microglia with different functions, harmful or protective. Interestingly, the present results show that nicotine exerts opposite effects on TNF release in response to LPS and ATP/BzATP; namely, it significantly inhibited massive TNF release, whereas it enhanced protective TNF release. Therefore, nicotine may regulate the release of TNF toward neuroprotection by suppressing inflammatory TNF (via TLR4) and by strengthening neuroprotective TNF (via $P2X_7$ receptors).

These modulatory effects of nicotine have been proved to occur through the activation of α7 AChRs in microglia. There are a number of reports describing the contribution of nAChRs to brain functions, including learning and memory (MacDermot et al., 1999), antinociception (Marubio et al., 1999), and neuroprotection (Messi et al., 1997; Laudenbach et al., 2002). Until recently, the common view was that α7 nAChRs were expressed mainly in neurons, but increasing evidence suggests that this type of nAChR is also expressed in non-neuronal cells and is implicated in the regulation of cell function and Ca^{2+} signalling (Buisson and Bertrand, 2002). In keratinocytes, for example, exposure to nicotine causes a reduction in cell migration (Zia et al., 2000), and, in astrocytes, nicotine modulates calcium signaling via calcium-induced calcium release (CICR; Sharma and Vijayaraghavan, 2001). More recently, it was revealed that α7 nAChRs are also expressed in mouse peritoneal macrophages and mouse brain microglia (Wang et al., 2003, 2004; Shytle et al., 2004). In this study, we also confirmed the expression of functional α7 nAChRs in rat primary cultured microglia, but they showed the unexpected properties.

Neuronal α7 nAChRs are typical ligand-gated ion channels; however, microglial α7 nAChRs seem to be different from those of their neuronal counterparts, which have a high permeability to Ca^{2+}. First, in microglia, nicotine induced an increase in intracellular Ca^{2+} concentrations even in the absence of extracellular Ca^{2+}. Second, nicotine-induced Ca^{2+} response was suppressed by chelating intracellular Ca^{2+} (with BAPTA-AM), by inhibiting PLC (with U73122) as well as by blocking the IP_3 receptor (with xestospongin C). In addition, the electrophysiological studies showed that currents could not be elicited by nicotine stimulation, although ATP-induced currents were detected in the same cells tested. These results suggest that microglial α7 nAChRs may not function as a ligand-gated ion channel but may be instead coupled to the activation of PLC and the mobilization of Ca^{2+} from IP_3-sensitive intracellular Ca^{2+} stores. Further studies will be required to clarify whether α7 nAChRs could activate PLC in the same manner as G protein-coupled receptors, as previously reported as a nonclassical nicotine receptor in frog pituitary melanotrophs (Garnier et al., 1994), or via another mechanism. Recently, Severance et al. (2004) reported the finding that α7 nAChRs have two isoforms, which may help to explain the multiplicity of α7 nAChRs. Such a new typed α7 nAChR isoform might be implicated in the diversity of signaling generated by nicotine.

All three members of MAP kinase family, ERK, JNK and p38, play key roles in the production of cytokines, including TNF (Bhat et al., 1998; Lee et al., 2000), but their roles are different. In LPS-stimulated microglia, as shown here, JNK and p38 mediate posttranscriptional steps of TNF production, whereas ERK is involved in the transcriptional regulation. Our results demonstrate that nicotine inhibited LPS-induced activation (phosphorylation) of JNK and p38, but not ERK, suggesting that nicotine may interfere with the posttranscriptional step of TNF synthesis by inhibiting the activation of JNK and p38. Consistently with this result, nicotine did not change TNF mRNA expression.

In the case of ATP stimulation, as we reported previously (Suzuki et al., 2004), all three MAP kinases play similar critical roles in TNF production; JNK and ERK regulate the transcription, and p38 is involved in the regulation of posttranscriptional steps, especially the export of TNF mRNA from nucleus to cytoplasm. Nicotine did not affect the activation of ERK, JNK, or p38 in ATP-stimulated microglia. Insofar as nicotine enhanced TNF release without promoting further mRNA expression, for at least 1 hour after stimulation, α7 nAChRs may stimulate the posttranscriptional process of TNF synthesis through an MAP kinase-independent pathway. To investigate further the mechanism underlying nicotine-induced increase in TNF release in $P2X_7$ receptor-activated-stimulated microglia, we measured BzATP-elicited Ca^{2+} signal after treating the cells with nicotine for 10 min at a concentration of 10 μM, which showed the maximal increasing effect on TNF release. This low concentration of nicotine did not induce detectable Ca^{2+} increase by itself but substantially increased the Ca^{2+} responses elicited by BzATP. We previously confirmed that the BzATP-induced increase in intracellular Ca^{2+} levels is due to Ca^{2+} influx through $P2X_7$ receptors, so nicotine may modulate $P2X_7$ receptor functioning by increasing its channel activities. $P2X_7$ receptor-mediated MAP kinase activation is independent of extracellular Ca^{2+} (Hide et al., 2000), in line with the present results showing that nicotine increased Ca^{2+} signal without affecting MAP kinase activation. The mechanism of interaction between α7 nAChR and $P2X_7$ receptors remains undefined.

Interestingly, macrophage α7 nAChRs play a critical role in the cholinergic antiinflammatory pathway, which

has been revealed after electrical stimulation of vagus nerve (Borovikova et al., 2000; Wang et al., 2003). Moreover, a similar antiinflammatory role of microglial α7 nAChRs in the mouse brain has been proposed (Shytle et al., 2004). Nicotine is a major component in tobacco, and it has been recognized that the incidence of neurodegenerative diseases such as Parkinson's disease is less in smokers, suggesting a neuroprotective role of nicotine (Picciotto and Zoli, 2002). Actually, it was shown that nicotine protects cortical neurons through neuronal α7 nAChRs, which transduce signals to the PI3K/Akt pathway in a cascade (Kihara et al., 2001). Our present results as well as the report by Shytle et al. (2004) may give an additional explanation for nicotine-induced neuroprotection from the view of the regulation of neuroinflammation. In addition, our data provide other evidence for a possible protective role of nicotine, in that nicotine may be capable of enhancing ATP-mediated neuroprotective TNF release by microglia.

In conclusion, we have provided new evidence for the existence of nonconventional α7 nAChRs in rat microglia. Although neuronal α7 nAChRs belong to ligand-gated ion channels, microglial α7 nAChRs may be coupled to the activation of PLC and evoke Ca^{2+} release from IP_3-sensitive Ca^{2+} stores. Such unique receptors should play an important role in neuroprotection, because the activation of these receptors is capable of modulating the stage of microglia from the overactive inflammatory type to a protective type. Therefore, it is conceivable that nicotinic receptor agonists that target α7 nAChRs in microglia may have significant therapeutic potential in neuroinflammatory diseases in the brain.

ACKNOWLEDGMENTS

We thank Prof. Shigeto Yamawaki, Department of Psychatry, Graduate School of Biomedical Sciences, Hiroshima Univeristy, and the Research Center for Molecular Medicine, Hiroshima University School of Medicine, for the use of Ca^{2+} imaging system. We also thank Dr. Faiz Kermani for his helpful comments. This study was supported by a Grant-in-Aid for Science Research from the Japanese Ministry of Education, Culture, Sports, Science and Technology and by a grant from the Japanese Smoking Research Association.

REFERENCES

Akiyama H, Barger S, Barnum S, Bradt B, Bauer J, Cole GM, Cooper NR, Eikelenboom P, Emmerling M, Fiebich BL, Finch CE, Frautschy S, Griffin WST, Hampel H, Hull M, Landreth G, Lue L, Mrak R, Mackenzie IR, McGeer PL, O'Banion MK, Pachter J, Pasinetti G, Plata-Salaman C, Rogers J, Rydel R, Shen Y, Streit W, Strohmeyer R, Tooyoma I, Van Muiswinkel FL, Veerhuis R, Walker D, Webster S, Wegrzyniak B, Wenk G, Wyss-Coray T. 2000. Inflammation and Alzheimer's disease. Neurobiol Aging 21:383–421.

Albuquerque EX, Pereira EF, Castro NG, Alkondon M, Reinhardt S, Schroder H, Maelicke A. 1995. Nicotinic receptor function in the mammalian central nervous system. Ann N Y Acad 757:48–72.

Aloisi F. 2001. Immune function of microglia. Glia 36:165–179.

Barone FC, Arvin B, White RF, Miller A, Webb CL, Willette RN, Lysko PG, Feuerstein GZ. 1997. Tumor necrosis factor-α: a mediator of focal ischemic brain injury. Stroke 28:1233–1244.

Bhat NR, Zhang P, Lee JC, Edward LH. 1998. Extracellular signal-regulated kinase and p38 subgroups of mitogen-activated protein kinases regulate inducible nitric oxide synthase and tumor necrosis factor-α gene expression in endotoxin-stimulated primary glial cultures. J Neurosci 18:1633–1641.

Borovikova LV, Ivanova S, Zhang M, Yang H, Botchkina GI, Watkins LR, Wang H, Abumrad N, Eaton JW, Tracy KJ. 2000. Vagus nerve stimulation attenuates the systemic inflammatory response to endotoxin. Nature 405:458–462.

Buisson B, Bertrand D. 2002. Nicotine addiction: the possible role of functional upregulation. Trends Pharmacol Sci 23:130–136.

Cheng B, Christakos S, Mattson MP. 1994. Tumor necrosis factors protect neurons against metabolic-excitotoxic insults and promote maintenance of calcium homeostasis. Neuron 12:139–153.

Cordero-Erausquin M, Marubio LM, Klink R, Changeux JP. 2000. Nicotine receptor function: new perspectives from knockout mice. Trends Pharmacol Sci 21:211–217.

Dajas-Bailador F, Wonnacott S. 2004. Nicotinic acetylcholine receptors and the regulation of neuronal signaling. Trends Pharmacol Sci 25:317–324.

Gao HM, Liu B, Zhang W, Hong JS. 2003. Novel anti-inflammatory therapy for parkinson's disease. Trend Pharmacol Sci 24:395–401.

Garnier M, Lamacz M, Tonin C, Vaudry H. 1994. Functional characterization of a nonclassical nicotine receptor associated with inositolphospholipid breakdown and mobilization of intracellular calcium pools. Proc Natl Acad Sci U S A 91:11743–11747.

Gary DS, Bruce-Keller AJ, Kindy MS, Mattson MP. 1998. Ischemic and excitotoxic brain injury is enhanced in mice lacking the p55 tumor necrosis factor receptor. J Cereb Flow Metab 18:1283–1287.

Hide I, Toriu N, Nuibe T, Inoue A, Hide M, Yamamoto S, Nakata Y. 1997. Suppression of TNF-α secretion by azelastine in a rat mast (RBL-2H3) cell line. J Immunol 159:2932–2940.

Hide I, Tanaka M, Inoue A, Nakajima K., Kohsaka S, Inoue K, Nakata Y. 2000. Extracellular ATP triggers tumor necrosis factor-α release from rat microglia. J Neurochem 75:965–972.

Kihara T, Shimohama S, Sawada H, Honda K, Nakamizo T, Shibasaki H, Kume T, Akaike A. 2001. α7 Nicotinic receptor transduces signals to phosphatidylinositol 3-kinase to block Aβ-amyloid-induced neurotoxicity. J Biol Chem 276:13541–13546.

Kim WG, Mohney RP, Wilson B, Jeohn GH, Liu B, Hong JS. 2000. Regional difference in susceptibility to lipopolysaccharide-induced neurotoxicity in the rat brain: role of microglia. J Neurosci 20:6309–6316.

Laudenbach V, Medja F, Zoli M, Rossi FM, Evrard P, Changeux JP, Gressens P. 2002. Selective activation of central subtypes of the nicotinic acetylcholoine receptor has opposite effects on neonatal excitotoxic brain injuries. FASEB J 16:423–425.

Lee YB, Schrader JW, Kim SU. 2000. p38 MAP kinase regulates TNF-α production in human astrocytes and microglia by multiple mechanisms. Cytokine 12:874–880.

Liu B, Hong JS. 2003. Role of microglia in inflammation-mediated neurodegenerative diseases: mechanisms and strategies for therapeutic intervention. J Pharmacol Exp Ther 304:1–7.

MacDermott AB, Role LW, Siegelbaum SA. 1999. Presynaptic ionotropic receptors and the control of transmitter release. Annu Rev Neurosci 22:443–485.

Marubio LM, del Mar Arroyo-Jimenez M, Cordero-Erausquin M, Lena C, Le Novere N, de Kerchove d'Exaerde A, Huchet M, Damaj MI, Changeux JP. 1999. Reduced antinociception in mice lacking neuronal nicotinic receptor subunits. Nature 398:805–810.

Matsubayashi H, Swanson KL, Albuquerque EX. 1997. Amantadine inhibits nicotinic acetylcholine receptor function in hippocampal neurons. J Pharmacol Exp Ther 281:834–844.

Matsubayashi H, Alkondon M, Pereira EFR, Swanson KL, Albuquerque EX. 1998. Strychnine: a potent competitive antagonist of α-bungarotoxin-sensitive nicotinic acetylcholine receptors in rat hippocampal neurons. J Pharmacol Exp Ther 284:904–913.

Matsubayashi H, Inoue A, Amano T, Seki T, Nakata Y, Sasa M, Sakai N. 2004. Involvement of α7- and α4β2-type postsynaptic nicotinic acetylcholine receptors in nicotine-induced excitation of dopaminergic neurons in the substantia nigra: a patch clamp and single-cell PCR study using acutely dissociated nigral neurons. Brain Res Mol Brain Res 129:1–7.

Messi ML, Renganathan M, Grigorenko E, Delbono O. 1997. Activation of α7 nicotinic acetylcholine receptor promotes survival of spinal cord motoneurons. FEBS Lett 411:32–38.

Nakajima K, Kohsaka S. 2004. Microglia: neuroprotective and neurotrophic cells in the central nervous system. Curr Drug Targets Cardiovasc Haematol Disord 4:65–84.

Nakajima K, Shimojo M, Hamanoue M, Shiura S, Sugita H, Kosaka S. 1992. Identification of elastase as a secretory protease from cultured rat microglia. J Neurochem 58:1401–1408.

Picciotto MR, Zoli M. 2002. Nicotinic receptors in aging and dementia. J Neurobiol 53:641–655.

Severance EG, Zhang H, Cruz Y, Pakhlevaniants S, Hadley SH, Amin J, Wecker L, Reed C, Cuevas J. 2004. The α7 nicotinic acetylcholine receptor subunit exists in two isoforms that contribute to functional ligand-gated ion channels. Mol Pharmacol 66:420–429.

Sharma G, Vijayaraghavan S. 2001. Nicotinic cholinergic signaling in hippocampal astrocytes involves calcium-induced calcium release from intracellular stores. Proc Natl Acad Sci U S A 98:4148–4153.

Sharma G, Vijayaraghavan S. 2002. Nicotine receptor signaling in nonexcitable cells. J Neurobiol 53:524–534.

Shigemoto-Mogami Y, Koizumi S, Tsuda M, Ohsawa K, Kohsaka S, Inoue K. 2001. Mechanisms underlying extracellular ATP-evoked interleukin-6 release in mouse microglial cell line, MG-5. J Neurochem 78:1339–1349.

Shohami E, Ginis I, Hallenbeck JM. 1999. Dual role of tumor necrosis factor alpha inbrain injury. Cytokine Growth Factor Rev 10:119–130.

Shytle RD, Mori T, Townsend K, Vendrame M, Sun N, Zeng J, Ehrhart J, Silver AA, Sanberg PR, Tan J. 2004. Cholinergic modulation of microglial activation by α7 nicotinic receptors. J Neurochem 89:337–343.

Suzuki T, Hide I, Ido K, Kohsaka S, Inoue K, Nakata Y. 2004. Production and release of neuroprotective tumor necrosis factor by $P2X_7$ receptor-activated microglia. J Neurosci 24:1–7.

Wang H, Yu M, Ochani M, Amella CA, Tanovic M, Susarla S, Li JH, Wang H, Yang H, Ulloa L, Al-Abed Y, Czura CJ, Tracey KJ. 2003. Nicotinic acetylcholine receptor α7 subunit is an essential regulator of inflammation. Nature 421:384–388.

Wang H, Liao H, Ochani M, Justiniani M, Lin X, Yang L, Al-Abed Y, Wang H, Metz C, Miller EJ, Tracey KJ, Ulloa L. 2004. Cholinergic agonists inhibit HMGB1 release and improve survival in experimental sepsis. Nat Med 10:1216–1221.

Zia S, Ndoye A, Lee TX, Webber RJ, Grando SA. 2000. Receptor-mediated inhibition of keratinocyte migration by nicotine involves modulations of calcium influx and intracellular concentrataion. J Pharmacol Exp Ther 293:973–981.

Pain 127 (2007) 161–172

PAIN

www.elsevier.com/locate/pain

NMDA receptor-independent synaptic plasticity in the central amygdala in the rat model of neuropathic pain

Ryo Ikeda [a,b], Yukari Takahashi [a], Kazuhide Inoue [c], Fusao Kato [a,*]

[a] *Laboratory of Neurophysiology, Department of Neuroscience, Jikei University School of Medicine, Minato-ku, Tokyo 105-8461, Japan*
[b] *Department of Orthopaedics, Jikei University School of Medicine, Minato-ku, Tokyo 105-8461, Japan*
[c] *Department of Molecular and System Pharmacology, Graduate School of Pharmaceutical Sciences, Kyushu University, 3-1-1 Maidashi, Higashi, Fukuoka 812-8582, Japan*

Received 31 March 2006; received in revised form 12 August 2006; accepted 5 September 2006

Abstract

Neurons in the latero-capsular part of the central nucleus of the amygdala (CeA), a region now called the "nociceptive amygdala", receive predominantly nociceptive information from the dorsal horn through afferent pathways relayed at the nucleus parabrachialis (PB). Excitatory synaptic transmission between the PB afferents and these neurons is reported to become potentiated within a few hours of the establishment of arthritic or visceral pain, making it a possible mechanism linking chronic pain and unpleasant negative emotional experiences. However, it remains unknown whether such synaptic potentiation is consolidated or becomes adaptively extinct in the longer-lasting form of chronic pain, such as neuropathic pain, an as yet serious and frequent type of pain of important clinical concern. To address this issue, we recorded postsynaptic currents in CeA neurons evoked by PB tract stimulation in acute brain slices from young rats with neuropathic pain, as evaluated by tactile allodynic responses, following unilateral spinal nerve ligature made 1 week earlier. CeA neurons contralateral to the nerve ligation showed significantly larger-amplitude postsynaptic currents than those in the ipsilateral CeA and sham- and non-operated groups. The degree of synaptic potentiation, as compared between two sides, was positively correlated to that of tactile allodynia responses. In addition, blockade of NMDA receptors did not affect this potentiation. We conclude that potentiation of the PB-CeA synapse is consolidated in long-lasting neuropathic pain but that this potentiation results from a molecular mechanism distinct from that in arthritic and visceral pain.

Keywords: Neuropathic pain; Amygdala; Excitatory postsynaptic currents; Nucleus parabrachialis; Tactile allodynia; Emotion; NMDA receptor

1. Introduction

Persistent chronic pain has a strong emotional component associated with negative affection (Price, 2002; McWilliams et al., 2003; Rhudy and Meagher, 2003). The amygdala, a key player in emotional responses to various sensory stimuli (Davis, 1998; LeDoux, 2000; Zald, 2003), is one of the principle structures linking pain sensation and emotional response as it receives pain-related information via the spino-parabrachio-amygdaloid pain pathway (Gauriau and Bernard, 2002). The nociceptive information arising from the superficial layers of the dorsal horn crosses the midline and forms synapses in the pontine parabrachial area (PB). From this area, an ascending projection reaches the central nucleus of the amygdala (CeA), in particular the latero-capsular part of the CeA, now called the "nociceptive amygdala" because of its abundance of nociceptive neurons (Bernard et al., 1992).

The amygdala is also associated with the synaptic plasticity underlying fear and painful memories in animals and humans (Maren, 2005; Phelps and LeDoux,

* Corresponding author. Tel.: +81 3 3433 1111 ext. 2395; fax: +81 3 3433 1279.
E-mail address: fusao@jikei.ac.jp (F. Kato).

0304-3959/$32.00
doi:10.1016/j.pain.2006.09.003

2005). Such plasticity also occurs with nociceptive inputs. For example, using acute-onset models of the arthritis and visceral pain models of the rat, Neugebauer and colleagues (2003; 2004) demonstrated that excitatory synaptic transmission and neuronal excitability in CeA are potentiated due to augmented NMDA receptor functions in brain slice preparations prepared 6–8 h after the generation of the pain models.

Another frequently observed form of chronic pain in human patients is neuropathic pain, resulting from various etiologies including cancer, diabetes-linked neuropathy and peripheral nerve injury (Russo and Brose, 1998; Woolf and Mannion, 1999; Scholz and Woolf, 2002). For these patients, the pain sensation is long lasting and seriously affects quality of life, including its emotional aspects, against which drug-based therapeutic strategy has yet to be established. Despite recent demonstrations that hyperexcitability of neurons in the dorsal horn of the spinal cord underlies neuropathic pain (Coull et al., 2003; Tsuda et al., 2003; Inoue et al., 2004; Coull et al., 2005), how neuropathic pain affects the emotional responses in the brain network remains unknown.

To address this issue, we examined whether synaptic transmission in the CeA is affected in an animal model of neuropathic pain, for the following reasons. First, in animal models, neuropathic pain can be quantitatively evaluated by measuring touch-induced allodynia, a form of hypersensitivity to tactile stimulation. Second, because the hypersensitivity to tactile stimuli is long lasting in animal models, it allows analysis over several days of the functional synaptic changes following a sustained increase in pain information reaching the amygdala, in turn allowing the examination of any distinct mechanisms underlying the plastic changes in the late phase of chronic pain, as occurs in hippocampal late-phase long-term potentiation (LTP) which involves molecular mechanisms distinct from early phase LTP (Nayak et al., 1998; Soderling and Derkach, 2000). Here, we report that the synaptic transmission mediated by non-NMDA receptors is potentiated in the CeA with high correlation to allodynia establishment in chronic (>6 days) pain models. A part of this work was previously presented in abstract form (Ikeda et al., 2005).

2. Methods

2.1. Neuropathic pain model

The manipulation of the animals was approved by the Animal Experiment Committee at the Jikei University School of Medicine and conformed to the Guiding Principles for the Care and Use of Animals in the Field of Physiological Sciences of the Physiological Society of Japan (1998) and to the guidelines of the International Association for the Study of Pain (Zimmermann, 1983). Young Wistar rats of either sex aged 20–26 days postnatal were used in this study. They were no older than 33 days postnatal at the time of electrophysiological recordings and we observed no systematic difference between the results from the male and female rats. The data from both sexes are therefore pooled in this study. Rats were anesthetized initially with diethyl ether and mounted on a surgical platform in a prone position with the limbs fixed. Anesthesia was then maintained with sevoflurane or isoflurane (1.5–2% in 100% O_2). A longitudinal incision (about 0.5 cm in length) was made at the midline of the lower lumbar using a sterile surgical blade. The left paraspinal muscles were isolated and the left L6 transverse process was exposed. Under a dissecting microscope, the left L6 transverse process covering the L4 and L5 spinal nerves was carefully removed. The left L5 spinal nerve was isolated and tightly ligated with 6–0 silk threads in the "ligation" group ($n = 39$), ligation was not performed in the "sham-operated" group ($n = 25$), and no surgical procedure was carried out in the "non-operated" group ($n = 13$). After surgery, the muscles were sutured in layers, the skin was closed using nylon thread (4–0), and anesthesia discontinued. Animals fully recovered from anesthesia within 1 h and showed no signs of distress as evidenced by the monitoring of breathing patterns, grooming behavior and locomotion in the cage. The rats were housed in cages filled with soft cushion-like flooring in a temperature- (around 25 °C) and humidity- (around 50%) controlled room. Water and food were available ad libitum and there was no observed difference in water and food consumption between the groups. Body weight measured at post-operational day 6–7 did not differ significantly between the ligation, sham-operated and non-operated groups ($P = 0.386$; ANOVA), at 75.6 ± 2.7 g (mean ± SEM; $n = 34$), 79.3 ± 2.0 g ($n = 25$) and 81.2 ± 5.2 g ($n = 13$), respectively. Behavior was monitored regularly and no aberrant symptoms arising from excessive nociception were observed except for a mild deformity of the lesioned paw (Kim and Chung, 1992), because of which, the von Frey filament test described below could not be conducted entirely in a blind manner. Every 1–2 days, rats were individually moved to a cage for measurement of the paw withdrawal threshold (see below), during which special care was taken to avoid noxious stimulation of the hindlimb. No aberrant responses were observed during interactions with the investigator.

2.2. von Frey filament test

The paw withdrawal threshold to mechanical stimuli was evaluated by well-trained experimenters according to the previously reported method (Tsuda et al., 2003). Mechanical stimuli were applied using von Frey filaments of different rigidities (0.4–15.0 g). Each rat was placed on a metal mesh floor (25 cm × 25 cm) and a von Frey filament was applied manually from beneath. The 50% threshold was estimated by the up and down method (Chaplan et al., 1994). Care was taken to reduce the number of trials to avoid unnecessary pain sensation. The tests were performed immediately before the operation and repeated every 1–2 days for all rats until the final test immediately before decapitation (Fig. 1).

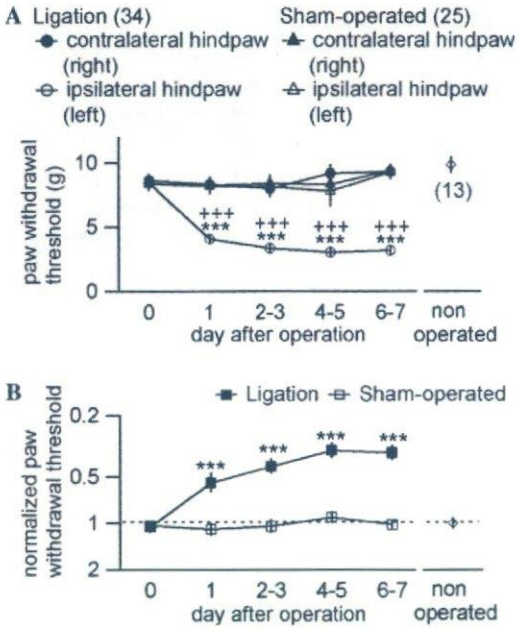

Fig. 1. Side-specific tactile allodynia after unilateral spinal nerve ligation. (A) Summary of the time-course of paw withdrawal threshold in the ligation, sham- and non-operated groups. Open and filled circles indicate responses in the hindpaws ipsilateral (left) and contralateral (right) to the ligation, respectively. Open and filled triangles show the responses in the hindpaws ipsilateral (left) and contralateral (right) to the sham-operation, respectively. Diamond shows the value from the non-operated group. Mean ± SEM. $^{***}P < 0.001$ vs. sham- and non-operated groups (ANOVA). $^{+++}P < 0.001$ vs. values before operation (measured at post-operational day 0; ANOVA). Numbers in parentheses indicate the number of rats. (B) Time course of the paw withdrawal threshold (value in the hindpaw ipsilateral to the ligation (left) is normalized by that in the hindpaw contralateral to the ligation (right) measured in the same rat). Filled and open squares indicate values from the ligation and sham-operated groups, respectively. Diamond shows that value from the non-operated group. Mean ± SEM. $^{***}P < 0.001$ vs. sham- and non-operated groups (Mann–Whitney U test).

2.3. Preparation of transverse brain slices

Immediately after the final von Frey filament test on post-operational day 6–7, the rats were decapitated under ketamine anesthesia (100–150 mg/kg, i.p.). In a subset of experiments ($n = 5$), rats were anesthetized with isoflurane (2–3% in 100% O_2) before decapitation to analyze the influence of ketamine anesthesia. We obtained both ipsilateral (left) and contralateral (right) coronal brain slices to the operation side (left) from the ligation group (69 unilateral slices from 34 rats), sham-operated group (51 unilateral slices from 25 rats) and non-operated group (33 unilateral slices from 13 rats) according to previously described procedures (Shigetomi and Kato, 2004; Ikeda and Kato, 2005). Briefly, the brain was dissected out and cut at the midline. The dissected hemisphere was secured on the cutting stage of a vibrating blade slicer (DSK-1000, Dosaka EM) with the rostral end upwards. Coronal slices of 400-μm thickness containing the amygdala were cut in the ice-cold cutting artificial cerebrospinal fluid (ACSF) composed of (in mM) 125 NaCl, 3 KCl, 0.1 $CaCl_2$, 5 or 3 $MgCl_2$, 1.25 NaH_2PO_4, 10 D-glucose, 0.4 L-ascorbic acid and 25 $NaHCO_3$ (pH 7.4 bubbled with 95% O_2 + 5% CO_2; osmolarity, ~310 mOsm/kg). The slices were first incubated in a holding chamber with a constant flow of standard ACSF, of which the concentrations of $CaCl_2$ and $MgCl_2$ were 2 and 1.3 mM, respectively, at 37 °C for 30–45 min. The slices were kept at room temperature (20–25 °C) in the same chamber until electrophysiological recording. Each slice was transferred to a recording chamber (~0.4-ml volume) and fixed with nylon grids to a platinum frame. The slice was submerged in and continuously superfused at a rate of 1–2 ml/min with standard ACSF. To isolate excitatory synaptic inputs, 100 μM picrotoxin (Sigma) and 1 μM strychnine HCl (Sigma) were dissolved in ACSF and bath-applied.

2.4. Patch-clamp recordings and cell visualization

Central amygdala (CeA) neurons were visually identified under an upright microscope (BX-50WI, Olympus) with infrared differential interference contrast (IR-DIC) optics. The IR-DIC images were captured using a chilled CCD camera (C5985-02, Hamamatsu Photonics) and stored digitally on a computer. The whole-cell transmembrane current was recorded from neurons in the left and right CeA (i.e., ipsilateral and contralateral, respectively, to the ligation). The patch-clamp electrodes were made from borosilicate glass pipettes (1B120F-4; World Precision Instruments). The composition of the internal solution was (in mM) 120 potassium gluconate, 6 NaCl, 1 $CaCl_2$, 2 $MgCl_2$, 2 ATPMg, 0.5 GTPNa, 12 phosphocreatine Na_2, 5 EGTA and 10 Hepes hemisodium (pH 7.2 as adjusted with KOH; osmolarity, ~310 mOsm/kg). The tip resistance of the electrode was 3–6 MΩ. The evoked excitatory postsynaptic currents (eEPSCs) were recorded at a holding potential of −70 mV. The membrane currents were recorded using an Axopatch 200B amplifier (Axon Instruments), low-pass filtered at 2 kHz and sampled at 4 kHz with a PowerLab interface (ADInstruments). To analyze the type of glutamate receptors involved, either 10 μM 6-cyano-7-nitroquinoxaline-2,3-dione (CNQX; Sigma; a non-NMDA receptor antagonist) or 50 μM D(−)-2-amino-5-phosphonopentanoic acid (APV; Sigma; a NMDA receptor antagonist) was dissolved in ACSF and bath-applied for more than 10 min. All recordings were made at room temperature (20–25 °C). The order of recordings from the right and left amygdala was randomized to avoid side-dependent differences due to changes in the viability of neurons during the time from slice preparation to recording. All compounds except those noted above were purchased from Sigma or Nacalai Tesque (Kyoto, Japan).

2.5. Afferent pathway stimulation

To activate action potential-dependent glutamate release from the afferent fibers arising from the PB and basolateral amygdala (BLA), under microscopic control we carefully located the stimulating electrode on the fiber tract dorsomedial to the CeA (PB tract) and in the BLA near the borderline to the CeA; "PB stimulation" and "BLA stimulation", respectively. To calculate the paired-pulse ratio of EPSCs as a measure of changes in presynaptic release properties (McKernan and Shinnick-Gallagher, 1997), double pulses with an interstimulus interval of 50 ms were delivered. The paired-pulse ratio (PPR) was calculated as the second EPSC amplitude (EPSC2) normalized by the first EPSC amplitude (EPSC1).

PB–CeA pathways showed paired-pulse facilitation (i.e., PPR > 1) in all neurons in a similar manner as that of a previous report (Neugebauer et al., 2003). Stimulation intensity was fixed at a sub-maximal value without spike current generation in the experiments examining the effects of glutamate receptor antagonists and in those for PPR measurement.

2.6. Data and statistical analysis

The recorded membrane current was analyzed off-line by an Igor Pro 5 (WaveMetrics, OR, USA) following procedures written by F.K. Peak amplitude was measured on the basis of the averaged waveform of eEPSCs (eight consecutive trials). Values are expressed as mean values ± standard error of the mean (SEM). Differences in the values were compared using one-way analysis of variance (ANOVA) followed by a post hoc test (Dunnet), the paired *t*-test and Mann–Whitney *U* test. Differences with a probability (*P*) less than 0.05 were considered significant.

3. Results

3.1. Side-specific establishment of tactile allodynia after unilateral spinal nerve ligation

A total of 72 rats were divided into the ligation ($n = 34$), sham-operated ($n = 25$) and non-operated ($n = 13$) groups. The paw withdrawal threshold was measured using von Frey filaments on post-operational day 0 in the ligation and sham-operated groups and immediately before the decapitation in the non-operated groups. The paw withdrawal threshold of the left hindlimb ipsilateral to the ligation decreased significantly at post-operational day 1 and remained decreased until post-operational day 6–7 (open circles in Fig. 1A). Such a decrease was not observed in the contralateral (right) hindlimb in the ligation group (filled circles in Fig. 1A) or in the bilateral hindlimbs in sham-operated rats (open and filled triangles in Fig. 1A), in which the paw withdrawal threshold gave consistently similar values to those in the non-operated group (diamond in Fig. 1A). These results indicate that animals that underwent spinal nerve ligation developed stable tactile allodynia within 1 week of operation, which is in good accordance with the results described by Kim and Chung (1992) who developed this neuropathic pain model. In addition, as there was no significant change in the paw withdrawal threshold in the right hindlimb contralateral to ligation on post-operational day 6–7 (filled circles in Fig. 1A), it is likely that the establishment of allodynia using this operative procedure is limited to the ipsilateral side to the ligation (i.e., the left side in the present experiments), at least within 1 week of operation in the rats at the ages used (see Discussion in Kim and Chung, 1992). Using these characteristics, we evaluated the degree of allodynia establishment in each rat, which varied from animal to animal, by normalizing the paw withdrawal threshold of the left hindlimb by that of the right hindlimb (ipsilateral/contralateral). Fig. 1B indicates the time-course of this "normalized paw withdrawal threshold" after operation in the different groups. The normalized paw withdrawal threshold did not change significantly from post-operational day 0–7 in the sham-operated group (open squares in Fig. 1B) and it was not significantly different from that in the non-operated group, but it significantly decreased in the ligation group to a mean value of 0.35 ± 0.04 on post-operational day 6–7 (filled squares in Fig. 1B). This result indicates that this normalized paw withdrawal threshold is a good index for the degree of side-specific tactile allodynia in each animal following unilateral nerve ligation.

3.2. Side-specific increase in the amplitude of EPSC evoked by PB–CeA pathway stimulation

Immediately following the final measurement of the paw withdrawal threshold on post-operational day 6–7, brain slices containing the amygdala were prepared for electrophysiological recordings. We recorded a total of 228 visually identified neurons in the capsular part of the CeA (Table 1). There was no apparent morphological difference in the amygdala nuclei or in the neurons as observed with IR-DIC optics between either side in the ligation, sham- and non-operated animals. There were also no differences between the groups in the ease with which good quality whole-cell recordings could be obtained from neurons. No significant difference was observed in the resting membrane potential or whole-cell capacitance between neurons from the right and left CeA in the ligation, sham- and non-operated groups

Table 1
Membrane properties of the CeA neurons recorded

	Ligation		Sham-operated		Non-operated
	Right CeA ($n = 53$)	Left CeA ($n = 52$)	Right CeA ($n = 43$)	Left CeA ($n = 36$)	($n = 44$)
Resting potential (mV)	−63.6 ± 0.9	−61.7 ± 0.8	−62.5 ± 0.8	−64.2 ± 1.0	−61.8 ± 1.0
Input resistance (MΩ)	147.8 ± 8.7	154.5 ± 8.0	169.4 ± 9.7	160.9 ± 9.7	166.4 ± 6.5
Cell capacitance (pF)	17.7 ± 0.8	16.9 ± 0.8	15.7 ± 0.9	16.1 ± 1.0	14.5 ± 0.7
Action potential threshold (mV)	−42.8 ± 0.7*	−41.1 ± 0.8	−39.9 ± 0.8	−39.4 ± 0.9	−37.3 ± 1.0

Values were measured immediately following establishment of the whole-cell mode. Mean ± SEM. *$P < 0.05$ vs. values in sham- and non-operated rats (ANOVA).

(Table 1). In contrast, the threshold membrane potential for action potential generation as measured by injecting depolarizing current under the current-clamp mode was significantly more hyperpolarized for neurons from the ligation group than from the sham- and non-operated groups. These data suggest that, as in the case of arthritic pain, some of the membrane properties of the CeA neurons are altered in the neuropathic pain model, but in a manner less manifest than in the arthritic pain models, which is accompanied by changes in resting membrane potential and input resistance (Neugebauer et al., 2003).

In the arthritic and visceral pain models, excitatory synaptic transmission at PB–CeA synapses is potentiated when measured 6–8 h after treatment (Neugebauer et al., 2003; Han and Neugebauer, 2004). We examined whether such plastic changes in CeA synaptic transmission occur in the longer-term neuropathic pain models. First, we stimulated the PB tract and recorded eEPSCs. When the stimulation intensity was gradually increased, PB tract stimulation gave rise to eEPSCs of larger amplitude with lower intensity in the right CeA (thick traces) than in the left CeA (thin traces) in the ligation group (Fig. 2A top). eEPSC amplitude in the right CeA of the ligation group was also significantly larger than that in the bilateral CeA in sham-operated rats (Fig. 2A bottom). In a large portion of slices, the larger amplitude of eEPSCs in the right CeA of the ligation group resulted in non-clamped spike-like fast inward current (thick trace in Fig. 2A top) at intensities of 500–1000 μA, whereas the neurons in the left CeA of the ligation group and in the bilateral CeA in sham-operated rats did not generate such spike-like currents with stimulation intensities lower than 1000 μA (see below for the stimulation intensity for action potential generation under the current-clamp mode; Fig. 3). Fig. 2B indicates the relation between intensity of the PB tract stimulation and eEPSC amplitude. From 100–600 μA, eEPSC amplitude in the right CeA neurons (filled circles in Fig. 2B) was significantly larger than that in the neurons belonging to other groups. There was no significant difference between neurons in the left CeA in the ligation group (open circles) and those in bilateral CeA in the sham- and non-operated groups (triangles and diamonds, respectively) at any stimulation intensity in the range of 50–4000 μA (Fig. 2B). These results strongly suggest that the potentiation of the PB–CeA transmission in the ligation group occurs in a manner highly restricted to the side receiving nociceptive information from the ligated side (i.e., the contralateral right CeA in the present experiments). We then evaluated the degree of synaptic potentiation in each animal by normalizing the eEPSC amplitude in the right CeA by that in the left CeA recorded from slices from the same rat. If several neurons ($n \leqslant 4$) were recorded from one side of a slice, their mean eEPSC value was used. This right/left

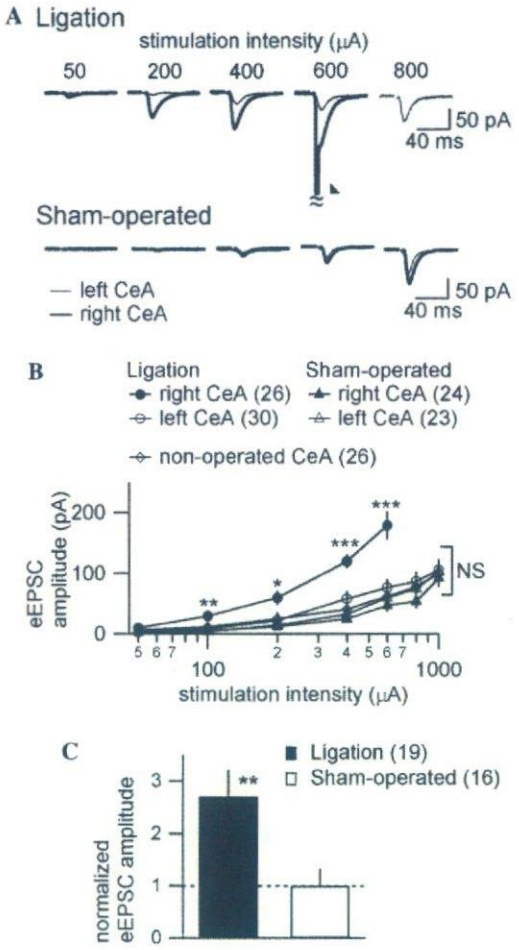

Fig. 2. EPSC evoked by PB tract stimulation in the CeA in neuropathic pain models. (A) Averaged waveforms of EPSCs evoked by PB tract stimulation at different intensities (average of eight consecutive responses). Top and bottom panels are recordings from neurons in the ligation and sham-operated groups, respectively. Thick and thin traces are recordings from neurons in the right and left CeA, respectively. (B) Relationship between stimulation intensity and eEPSC amplitude. Circles, triangles and diamonds indicate values from neurons in the ligation, sham-operated and non-operated groups, respectively. Mean ± SEM. Open and filled symbols indicate values from neurons in the left and right CeA, respectively. $^{*}P < 0.05$; $^{**}P < 0.01$; $^{***}P < 0.001$ compared to the left CeA in the ligation group, and to bilateral CeA in the sham- and non-operated groups (ANOVA). NS, not significantly different between groups (ANOVA). Numbers in parentheses indicate the number of neurons. (C) Summary of the normalized eEPSC amplitude (eEPSC amplitude in the right CeA normalized by that in the left CeA from the same rat) in the ligation (filled bar) and sham-operated (open bar) groups. eEPSCs were evoked by 400-μA stimulation. $^{**}P < 0.01$ vs. sham-operated group (Mann–Whitney U test). Numbers in parentheses indicate the number of rats.

ratio of eEPSC amplitude ("normalized eEPSC amplitude") was significantly larger in the ligation group than in the sham-operated group (Fig. 2C). In addition, this ratio was ~1 in the sham-operated group (Fig. 2C), suggesting that the significant and marked difference in eEPSC amplitudes between right and left CeA in the

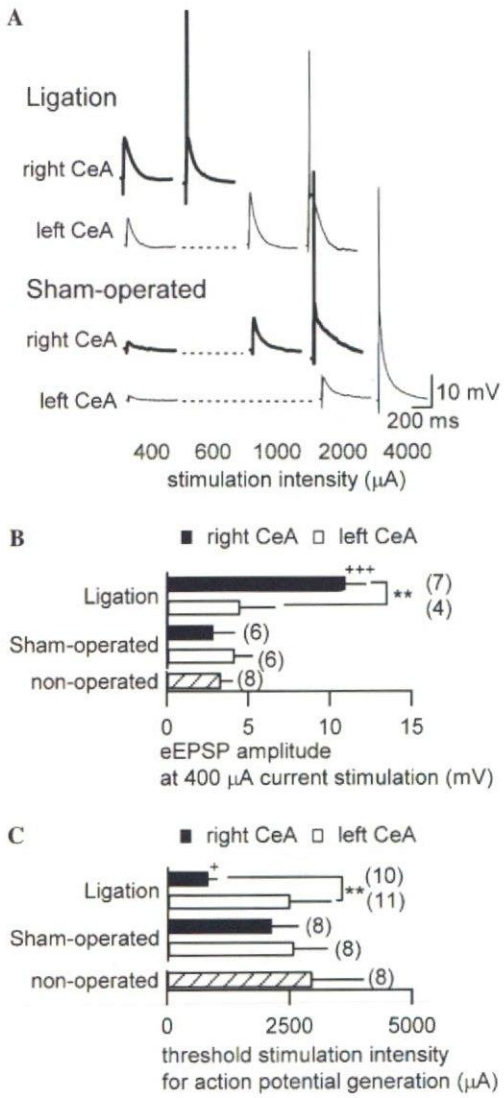

Fig. 3. EPSP and action potential generation by PB tract stimulation in the CeA in neuropathic pain models. (A) Averaged waveforms of EPSPs evoked by PB tract stimulation at different intensities (average of eight consecutive responses). Top and bottom panels are recordings from the ligation and sham-operated groups, respectively. Thick and thin traces show the membrane potential recording from the right and left CeA, respectively, from the same rat. (B) The summary of EPSP amplitude evoked by PB tract stimulation at 400-μA stimulation. Open and filled bars indicate values from neurons in the left and right CeA, respectively. Hatched bar indicates the value from bilateral neurons in non-operated rats. $^{**}P < 0.01$ vs. left CeA in the ligation group; $^{+++}P < 0.001$ compared to other groups (ANOVA). Numbers in parentheses indicate the number of neurons. (C) Summary of the threshold stimulation intensity for action potential generation in CeA neurons. Open and filled bars indicate values from neurons in the left and right CeA, respectively. Hatched bar indicates the value from bilateral neurons in non-operated rats. $^{**}P < 0.01$ compared to the left CeA in the ligation group; $^{+}P < 0.05$ compared to other groups (Mann–Whitney U test). Numbers in parentheses indicate the number of neurons.

ligation group does not primarily result from the asymmetric nature of the PB–CeA connection or from the asymmetry inherent in the recording and stimulation systems. Rather, it is likely that the synaptic potentiation in CeA was highly dependent on the side relative to the nociceptive input.

Does such synaptic potentiation in the contralateral (right) CeA in the ligation group affect the synaptic excitability of the CeA neurons? To directly address this issue, we recorded the membrane potential of the neurons under the current-clamp mode. When the intensity of the PB tract stimulation was increased, neurons in the right CeA in the ligation group generated action potential at a lower intensity than those in the left CeA as well as in those in sham-operated rats (Fig. 3A). In accordance with the above eEPSC data, the amplitude of evoked EPSP (eEPSP) was significantly larger in the right CeA in the ligation group than in the other groups (Fig. 3B), which resulted in a significantly lower minimum stimulation intensity required to make the postsynaptic neurons fire in the right CeA neurons (Fig. 3C). These results strongly indicate that such potentiated excitatory synaptic transmission facilitates the PB–CeA input to excite the neurons postsynaptic to the CeA neurons in a manner specific to the side receiving increased nociceptive information.

3.3. Increase in the amplitude of EPSC evoked by BLA-CeA pathway stimulation was less side-specific

The CeA neurons also receive strong excitatory inputs from the BLA, which transmits polymodal integrated sensory information originating in higher structures such as the thalamus and cortex (Shi and Davis, 1999; Sah et al., 2003; Pare et al., 2004). The striking difference between these reported models is that both PB–CeA and BLA–CeA transmissions are enhanced in the arthritis pain model, whereas BLA–CeA transmission is unaffected in the visceral pain model (Han and Neugebauer, 2004). It is therefore conceivable that enhancement of BLA–CeA transmission depends on the type of pain.

Stimulation of the ventrolateral pathway arising from the BLA resulted in eEPSC in CeA neurons. The BLA stimulation evoked EPSCs of larger amplitude in the neurons in the right CeA (Fig. 4A top, thick traces) than those in the left CeA (thin traces). In addition, in the majority of the left CeA neurons, the eEPSC amplitude was larger than that recorded in sham-operated rats (Fig. 4A top and bottom). Fig. 4B indicates the summary data of the amplitude of BLA–CeA eEPSC in response to increasing stimulation intensity. The amplitude of BLA–CeA eEPSC in the right CeA neurons in the ligation group (filled circles in Fig. 4B) was significantly larger than that in the left CeA neurons in the ligation group than that in the sham- and non-operated groups at 100–600 μA stimulation. However, unlike in PB–CeA transmission, the amplitude of BLA–CeA eEPSC in the left CeA neurons in the ligation group

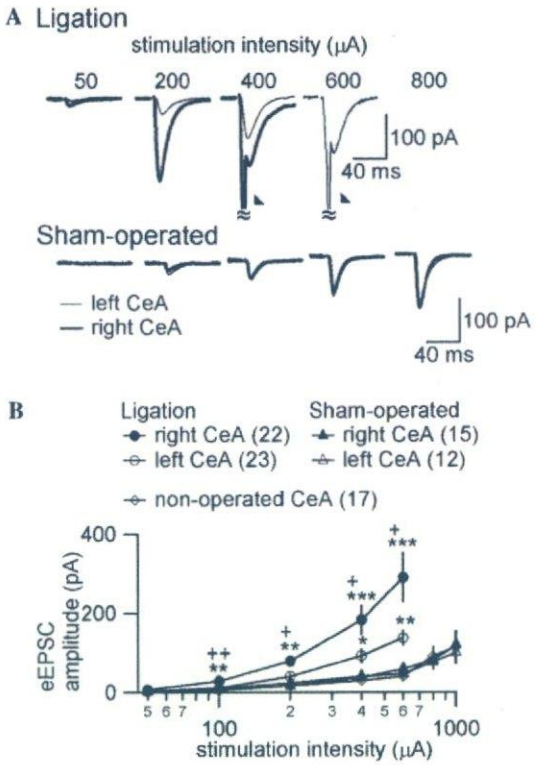

Fig. 4. EPSC evoked by BLA stimulation in the CeA in neuropathic pain models. (A) Averaged waveforms of EPSCs evoked by BLA stimulation at different intensities (average of eight consecutive responses). Top and bottom panels are recordings from neurons in the ligation and sham-operated groups, respectively. Thick and thin traces are recordings from neurons in the right and left CeA, respectively. (B) Relationship between stimulation intensity and eEPSC amplitude. Circles, triangles and diamonds indicate values from neurons in the ligation, sham-operated and non-operated groups, respectively. Mean ± SEM. Open and filled symbols indicate values from neurons in the left and right CeA, respectively. $^{*}P < 0.05$; $^{**}P < 0.01$; $^{***}P < 0.001$ vs. sham- and non-operated groups; $^{+}P < 0.05$; $^{++}P < 0.01$ vs. left CeA in the ligation group (ANOVA). Numbers in parentheses indicate the number of neurons.

(open circles in Fig. 4B) was also significantly larger than in the sham- and non-operated rats at intensities larger than 400 μA (triangles and diamonds, respectively, in Fig. 4B). These results indicate that, despite the difference in degree, BLA–CeA transmission is enhanced in both CeAs contra and ipsilateral to the ligation in the neuropathic pain models, suggesting that synaptic potentiation in the BLA–CeA pathway is less side-specific than that in the PB–CeA pathway. As with the PB–CeA synapse, the increased BLA–CeA eEPSC in the ligation group also resulted in eEPSP of larger amplitude that generated postsynaptic firing at significantly lower stimulation intensity than in the sham- and non-operated groups (data not shown). Because the eEPSC amplitude in response to BLA stimulation was increased in both sides of the CeA, the contralateral/ipsilateral ratio ("normalized eEPSC amplitude") would not represent the degree of side-specific potentiation in each rat and was therefore not estimated for the BLA–CeA transmission.

3.4. Increase in evoked EPSC amplitude at PB–CeA was positively correlated with the establishment of tactile allodynia

The above results indicate that in animal models of neuropathic pain, both the allodynic responses in vivo and synaptic transmission in the CeA in vitro are increased in a side-specific manner. There are, however, considerable rat-to-rat variations in these phenomena. If these two types of post-operative changes are mutually related, behavioral and electrophysiological changes in each rat would be expected to be correlated. We examined this hypothesis by analyzing the correlation between changes in eEPSC amplitude and changes in paw withdrawal threshold (Fig. 5). The values of normalized eEPSC amplitude by PB tract stimulation (eEPSC amplitude in the right CeA normalized by that in the left CeA, as plotted in Fig. 2C) at the highest stimulus intensity not evoking the spike currents in the slices from a rat were plotted against those obtained for the normalized paw withdrawal threshold (as plotted in Fig. 1B) at post-operational day 6–7 in the same rat (Fig. 5). The correlation coefficient between these variables was 0.75 ($P < 0.001$; $n = 26$; Spearman's rank correlation), indicating that the increase in PB–CeA synaptic transmission in the right CeA contralateral to the ligation is positively correlated to the side-dependent increase in allodynic responses in the neuropathic pain models. In contrast, the correlation coefficient between the normalized eEPSC amplitude induced by BLA stimulation and the normalized paw withdrawal threshold in

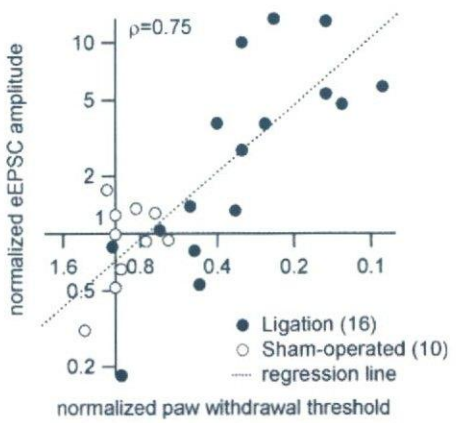

Fig. 5. Correlation between tactile allodynia and synaptic potentiation. A correlogram between the degree of tactile allodynia established and that of the PB–CeA transmission potentiation. Abscissa, the normalized paw withdrawal threshold (see Fig. 1); ordinate, the normalized eEPSC amplitude (see Fig. 2). Open and filled circles are values from the sham-operated ($n = 16$) and ligation ($n = 10$) groups, respectively. Dotted line indicates the linear regression line estimated by curve fitting ($\log[y] = 1.19\log[x] - 0.16$).

each rat was much smaller and not significant ($\rho = 0.40$; $P = 0.06$; $n = 23$).

3.5. Blockade of NMDA receptors did not affect the potentiated PB-CeA transmission in the neuropathic pain models

We further analyzed the mechanisms underlying this activity-dependent side-specific potentiation of PB–CeA transmission in the neuropathic pain models. The potentiation of PB–CeA transmission measured 6–8 h after establishment of acute arthritis in the rat is due to an increased NMDA receptor-mediated postsynaptic component, which is otherwise blocked by Mg^{2+} but becomes manifest even at a membrane potential of −60 mV in arthritis models (Bird et al., 2005). In their report, eEPSC was not abolished by CNQX, a non-NMDA receptor antagonist, in the arthritis CeA, unlike in the control CeA, and the synaptic potentiation was not observed after application of APV, a NMDA receptor antagonist, in the amygdala slices. Therefore, we examined whether a similar mechanism involving NMDA receptor-mediated transmission underlies the synaptic potentiation in the CeA of long-term neuropathic pain models. Two sets of evidence clearly indicate that this synaptic potentiation does not result from enhanced NMDA receptor function. First, with a holding potential of −70 mV, CNQX (10 μM) almost completely abolished PB–CeA eEPSC (Fig. 6A) in both sides of the CeA in the ligation and sham-operated groups. Only the stimulation artifact (Fig. 6A) and a noise-level component remained in the presence of CNQX in all groups (Fig. 6A2). This result is in contrast to the results of Bird et al. (2005) who reported that in the arthritic rats, a significant amount of PB–CeA EPSC remained in the presence of CNQX (30 μM). Second, application of APV (50 μM; ~10 min) did not significantly affect the amplitude of PB–CeA EPSC with 400 μA stimulation in both sides of the CeA in the ligation group (Fig. 6B1 and 2). The EPSC amplitude of the neurons from the right CeA was still markedly larger than that from the left CeA even in the presence of APV (Fig. 6B), indicating that the marked right-left difference in EPSC amplitude primarily resulted from the increased non-NMDA receptor component in the right CeA. It is unlikely that the negligible contribution of the NMDA receptor-mediated component resulted from the ketamine anesthesia used before decapitation, because very similar responses to APV (50 μM) were observed in five rats with strong allodynic responses being anesthetized with isoflurane prior to decapitation at post-operational day 6–7 (Fig. 6B). Our results strongly argue against the major involvement of an augmented NMDA receptor current in PB–CeA synaptic potentiation in neuropathic pain, unlike in the arthritis pain models. Rather, it is likely that the potentiation

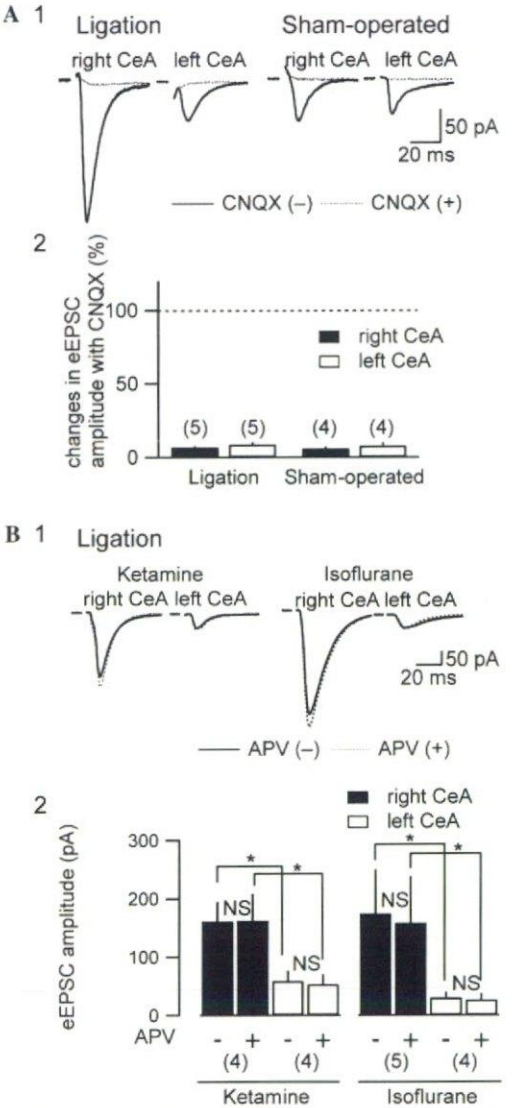

Fig. 6. NMDA receptor-independent synaptic plasticity in PB–CeA transmission in the rat model of neuropathic pain. (A1) Averaged waveforms of EPSCs evoked by PB tract stimulation in the absence (solid curves) and presence (broken curves) of CNQX (10 μM) (average of eight consecutive responses). Left and right panels show membrane currents recorded from neurons in bilateral CeAs in the ligation and sham-operated groups, respectively. (A2) Summary of the effect of CNQX on eEPSC amplitude. Filled and open bars indicate changes in eEPSC amplitude in the right and left CeA, respectively. Mean ± SEM. Numbers in parentheses indicate the number of neurons. (B1) Averaged waveforms of EPSCs evoked by PB tract stimulation in the absence (solid line) and presence (broken line) of APV (50 μM) in the ligation group (average of eight consecutive responses). Left and right two panels are the data from CeA neurons from two rats in which ketamine and isoflurane anesthesia, respectively, were used before decapitation. (B2) Summary of the effect of APV on eEPSC amplitude of the neurons in the right (filled bars) and left (open bars) CeA recorded before addition of APV (−) and in the presence of APV (+). Ketamine and isoflurane indicate the data from the rats in which ketamine and isoflurane were used before decapitation. Mean ± SEM. NS, not significantly different between eEPSC amplitudes in the absence and presence of APV (paired *t*-test). $^*P < 0.05$, Significantly different between the right and left CeA. Numbers in parentheses indicate the number of neurons.

of PB–CeA transmission in the neuropathic pain models involves enhanced non-NMDA receptor-mediated transmission.

3.6. Potentiation of PB–CeA synaptic transmission does not involve changes in the presynaptic release properties

The above results suggest that increased EPSC amplitude in the right CeA in the ligation group might result from postsynaptic alterations in the non-NMDA receptor-mediated transmission by increased nociceptive afferents from the PB. However, it is also possible that the properties of glutamate release from the presynaptic termini of the PB tract might play a role. To examine whether the potentiated transmission involves changes in the release properties, we analyzed the short-term plasticity of PB–CeA transmission, which is reported to show a strong short-term facilitation (Neugebauer et al., 2003). The PB tract was stimulated twice with an interval of 50 ms (Fig. 7A) in the right and left CeA in the ligation (left in Fig. 7A) and sham-operated (right in Fig. 7A) groups. Short-term facilitation of a similar intensity was observed in both sides and in both groups (Fig. 7A bottom). The PPR (EPSC2/EPSC1) did not significantly differ between either side or between the two groups (Fig. 7B). It is therefore unlikely that changes in the presynaptic release properties play a principal role in the pain-related plastic changes in PB–CeA transmission.

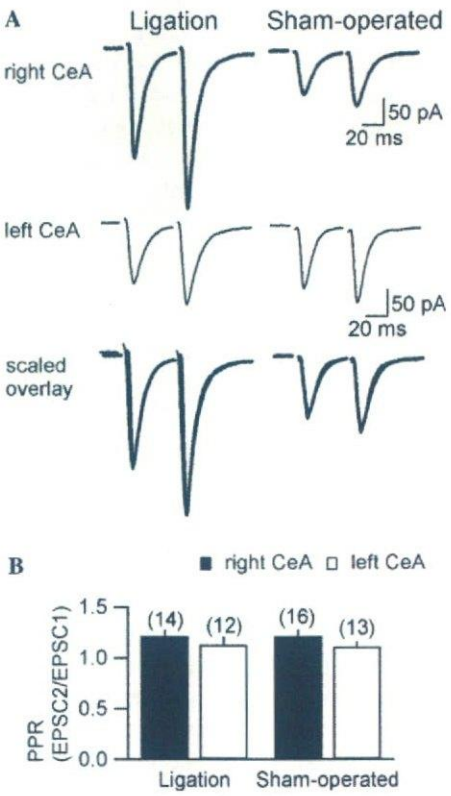

Fig. 7. Responses to paired-pulse stimulation of the PB tract of CeA neurons. (A) Averaged waveforms ($n = 8$) of EPSCs evoked by a paired stimulation of the PB tract at 50-ms intervals. Left and right panels show the membrane currents recorded from CeA neurons in the ligation and sham-operated groups, respectively. Top, typical recordings from neurons in the right CeA; middle, those in the left CeA; bottom, overlaid display of the responses in the right and left CeA scaled to the peak. Note the ratio of the second peak amplitude to the first peak amplitude is almost the same for groups and sides. (B) Summary of the paired-pulse ratio (the amplitude of the second eEPSC (EPSC2) normalized by the first eEPSC (EPSC1)). No significant difference between the groups was detected ($P = 0.566$; ANOVA). Numbers in parentheses indicate the number of neurons.

4. Discussion

4.1. Particularities of CeA synaptic potentiation in neuropathic pain models

Using the spinal nerve ligation model of neuropathic pain (Kim and Chung, 1992) and electrophysiological evaluation of the synaptic transmission in the CeA, here we present the following novel findings. (1) In animal models of long-lasting chronic neuropathic pain, excitatory synaptic transmission at the PB–CeA synapses is potentiated such that the neurons in the latero-capsular part of the CeA fire with a weaker PB input. (2) This potentiation occurs predominantly in the PB–CeA synapses contralateral to the peripheral neuropathic pain. (3) The degree of synaptic potentiation, as compared between the two sides, was positively correlated to the degree of enhanced tactile allodynia in the hindlimb with neuropathic pain. (4) This potentiation, unlike in the semi-chronic arthritis pain model, does not involve potentiation of the NMDA receptor-mediated component of the postsynaptic current but instead involves enhancement of the postsynaptic non-NMDA receptor-mediated component. (5) The BLA–CeA transmission was also potentiated in these chronic neuropathic models but in a less side-dependent manner. Together these results point to the pivotal role of the long-lasting potentiation of synapses in the "nociceptive amygdala" in chronic pain-related emotional behaviors.

The potentiation of PB–CeA synaptic transmission in the neuropathic pain model is in good accordance with that in the arthritis and visceral pain models as pioneered by Neugebauer and colleagues (Neugebauer et al., 2004). However, the present results advance our knowledge along several lines and we discuss these issues below.

4.2. Positive correlation between tactile allodynia and synaptic potentiation

First, taking advantage of this model which allows the degree of chronic neuropathic pain to be quantitatively evaluated by measuring the tactile allodynia threshold in each side of the hindlimbs, we demonstrated for the first time, a positive correlation

between allodynia establishment and synaptic potentiation. Such quantitative evaluation of tactile allodynia has been successfully used in the evaluation of neuropathic pain (Chapman et al., 1998) and is known to reflect sensitively the effects of drugs acting on the spinal nociceptive systems (Tsuda et al., 2003). In addition, the laterality-specific nature of this spinal cord–PB–CeA projection (see Gauriau and Bernard, 2002) enabled direct comparison between the painful and intact sides.

This positive correlation indicates that the synaptic potentiation of PB–CeA transmission depends on the intensity of nociceptive information of spinal origin. The tactile allodynia results from aberrant activation of nociceptive neurons in the spinal cord by tactile sensation that normally does not evoke nociception (Woolf and Mannion, 1999). It might therefore be possible that, in the neuropathic rats, simple touches of the hindpaw of the ligated side on the floor evoked allodynic nociception and activated the spino-parabrachio-amygdaloid pathways more frequently. It is thus likely that the increased sustained nociceptive signals from the spinal cord carried to the CeA via the PB triggered the side-specific synaptic potentiation in the CeA. The mechanism underlying this activity-dependent plasticity is an interesting subject for future study.

4.3. NMDA receptor-independent potentiation

The second particularity of the present results is the absence of NMDA receptor potentiation. This is in a marked contrast to the synaptic potentiation of PB–CeA synapses in semi-chronic arthritis pain models, which was occluded by NMDA receptor blockade in slice preparations (Bird et al., 2005). In the present chronic neuropathic pain model, potentiation was almost entirely dependent on the enhanced non-NMDA receptor-mediated transmission as evidenced by complete suppression with CNQX and the lack of a significant effect of APV on eEPSC amplitude in the ligation group. The marked difference in eEPSC amplitudes between the right and left CeA even in the presence of APV, which did not significantly affect the eEPSC amplitude, both in rats anesthetized with ketamine and with isoflurane before decapitation, indicates that enhancement of the NMDA component plays a limited, if any, role in the potentiated transmission in the chronic neuropathic pain model, despite some differences in recording conditions between their study and ours. This characteristic is reminiscent of late-phase LTP in the hippocampal CA1 in which de novo insertions of the AMPA receptors at the postsynaptic membrane give rise to potentiated synaptic transmission in an activity-dependent manner (Nayak et al., 1998). The most obvious difference between our study and that by Bird et al. (2005) is the duration after the pro-nociceptive manipulations (a few hours vs. about 1 week). It is therefore likely that the differences in the NMDA receptor contribution between these distinct models result from time-dependent alterations in the molecular mechanism underlying synaptic potentiation. A possible schema to explain such time-dependent alteration is as follows: (i) increased afferent activity from the PB due to increased nociception induces early phase synaptic potentiation through a mechanism that is common to the early onset synaptic potentiation in arthritic pain models involving CGRP receptor activation and NMDA receptor phosphorylation (Bird et al., 2005; Han et al., 2005) and/or through an unidentified mechanism specific to neuropathic pain, and (ii) sustained early phase potentiation for several days in neuropathic pain leads to late-phase potentiation that involves a switch from potentiated NMDA receptor function to enhanced non-NMDA receptor-mediated transmission, thus consolidating synaptic plasticity. This interpretation is consistent with the view that different molecular mechanisms participate in distinct steps of long-term potentiation in the central synapses, including those involved in early and late hippocampal LTP (Soderling and Derkach, 2000). This finding is of particular importance in the development of novel therapeutic approaches against neuropathic pain and related emotional disorders at various stages of chronic pain in human patients.

4.4. Distinct pathway-dependence of CeA synaptic potentiation in neuropathic pain

In the present study, unilateral neuropathic pain potentiated contralateral PB–CeA transmission and, to a lesser extent, bilateral BLA–CeA transmission. While visceral pain predominantly potentiates PB–CeA transmission, arthritic pain potentiates both the PB–CeA and BLA–CeA pathways (Neugebauer et al., 2003), indicating that the pain-related synaptic plasticity in the CeA depends both on the type of pain and on the pathway. CeA receives inputs from other amygdala nuclei and from the thalamus and cortex via the BLA (Pare et al., 2004) as well as from the spino-PB pathway via the PB tract (Bernard and Besson, 1990; Jasmin et al., 1997); the former carries highly processed polymodal sensory information and the latter carries nociception-specific information (Gauriau and Bernard, 2002; Neugebauer et al., 2004). It is conceivable that the difference in the pattern of synaptic potentiation in the CeA between different models of pain stems principally from the differences in the site and pathway at which the nociceptive information is generated and sent to the brain.

Unlike in arthritis pain induced by kaolin and carrageenan injection to the knee joint (Neugebauer et al., 2003) and in visceral colitis pain induced by intracolonal zymosan injection (Han and Neugebauer, 2004; Yu et al., 2005), in neuropathic pain as used in this study, nociception occurs through aberrant activation of noci-

ceptive neurons in the dorsal horn (Woolf et al., 1992; Tsuda et al., 2003; Inoue et al., 2004; Coull et al., 2005) and does not arise from the site of perceived pain (in the present case, the hindpaw). It is therefore likely that the sensory and nociceptive components of the allodynic sensation are dissociated and processed by specific pathways in neuropathic pain models, resulting in the specific patterns of synaptic potentiation in the CeA neurons.

Another issue to be noted in the present study is that ligation was made in the left spinal nerve and synaptic potentiation was observed in the right amygdala. In vivo and in vitro studies to date have reported no lateral specificity in the spino-brachio-amygdaloid pathways (Gauriau and Bernard, 2002; Neugebauer et al., 2003, 2004). However, several studies in the rat demonstrated that the right amygdala plays a greater role than the left amygdala in the acquisition and expression of certain forms of emotional memories (Baker and Kim, 2004; Scicli et al., 2004; Adamec et al., 2005; LaLumiere and McGaugh, 2005), in a similar manner to those found in humans and cats. Therefore an interesting topic for future research is to investigate whether such long-lasting potentiation of PB–CeA transmission occurs specifically in the right amygdala, which might have a greater impact on the emotional responses of the animal.

The amygdala is composed of several anatomically and functionally distinct nuclei (Sah et al., 2003). The CeA serves as the output nucleus for major amygdala functions. Localized lesion experiments have demonstrated that the roles played by the CeA and BLA are distinct in chemical somatic and visceral pains (Tanimoto et al., 2003), appetitive emotional learning (Parkinson et al., 2000), fear-conditioned behavior (Killcross et al., 1997) and Pavlovian second-order conditioning (Hatfield et al., 1996). The behavioral consequence of the distinct activation patterns of the PB–CeA and BLA–CeA pathways in the neuropathic pain models was not addressed in this study, however, identification of the downstream effects of such differential potentiation of these pathways will lead to the development of efficient therapeutic strategies against intractable chronic pain accompanied by emotional problems in human patients.

Acknowledgements

This work was supported in part by Grants for the Research on Health Sciences focusing on Drug Innovation from The Japan Health Sciences Foundation (KH21006) and Grants-in-Aid from the Ministry of Education, Culture, Sports, Science and Technology, Japan (Nos. 17023042, 17650116 and 17300123) to F.K. The authors thank Dr. Makoto Tsuda for advice on neuropathic pain models and allodynia measurements, and Drs. Eiji Shigetomi and Yutaka Yasui for critical reading of the manuscript. The expert assistance of T. Matsuo during the preparation of the manuscript and during the experiments is acknowledged.

References

Adamec R, Blundel J, Burton P. Role of NMDA receptors in the lateralized potentiation of amygdala afferent and efferent neural transmission produced by predator stress. Physiol Behav 2005;86:75–91.

Baker KB, Kim JJ. Amygdalar lateralization in fear conditioning: evidence for greater involvement of the right amygdala. Behav Neurosci 2004;118:15–23.

Bernard JF, Besson JM. The spino(trigemino)pontoamygdaloid pathway: electrophysiological evidence for an involvement in pain processes. J Neurophysiol 1990;63:473–90.

Bernard JF, Huang GF, Besson JM. Nucleus centralis of the amygdala and the globus pallidus ventralis: electrophysiological evidence for an involvement in pain processes. J Neurophysiol 1992;68:551–69.

Bird GC, Lash LL, Han JS, Zou X, Willis WD, Neugebauer V. Protein kinase A-dependent enhanced NMDA receptor function in pain-related synaptic plasticity in rat amygdala neurones. J Physiol 2005;564:907–21.

Chaplan SR, Bach FW, Pogrel JW, Chung JM, Yaksh TL. Quantitative assessment of tactile allodynia in the rat paw. J Neurosci Methods 1994;53:55–63.

Chapman V, Suzuki R, Dickenson AH. Electrophysiological characterization of spinal neuronal response properties in anaesthetized rats after ligation of spinal nerves L5-L6. J Physiol 1998;507:881–94.

Coull JA, Beggs S, Boudreau D, Boivin D, Tsuda M, Inoue K, Gravel C, Salter MW, De Koninck Y. BDNF from microglia causes the shift in neuronal anion gradient underlying neuropathic pain. Nature 2005;438:1017–21.

Coull JA, Boudreau D, Bachand K, Prescott SA, Nault F, Sik A, et al. Trans-synaptic shift in anion gradient in spinal lamina I neurons as a mechanism of neuropathic pain. Nature 2003;424:938–42.

Davis M. Anatomic and physiologic substrates of emotion in an animal model. J Clin Neurophysiol 1998;15:378–87.

Gauriau C, Bernard JF. Pain pathways and parabrachial circuits in the rat. Exp Physiol 2002;87:251–8.

Han JS, Li W, Neugebauer V. Critical role of calcitonin gene-related peptide 1 receptors in the amygdala in synaptic plasticity and pain behavior. J Neurosci 2005;25:10717–28.

Han JS, Neugebauer V. Synaptic plasticity in the amygdala in a visceral pain model in rats. Neurosci Lett 2004;361:254–7.

Hatfield T, Han JS, Conley M, Gallagher M, Holland P. Neurotoxic lesions of basolateral, but not central, amygdala interfere with Pavlovian second-order conditioning and reinforcer devaluation effects. J Neurosci 1996;16:5256–65.

Ikeda R, Kato F. Early and transient increase in spontaneous synaptic inputs to the rat facial motoneurons after axotomy in isolated brainstem slices of rats. Neuroscience 2005;134:889–99.

Ikeda R, Fujii K, Kato F. Neuropathic pain-related synaptic plasticity in the central amygdala neurons. Neurosci Res 2005;52(Suppl.):S200.

Inoue M, Rashid MH, Fujita R, Contos JJ, Chun J, Ueda H. Initiation of neuropathic pain requires lysophosphatidic acid receptor signaling. Nat Med 2004;10:712–8.

Jasmin L, Burkey AR, Card JP, Basbaum AI. Transneuronal labeling of a nociceptive pathway, the spino-(trigemino-)parabrachio-amygdaloid, in the rat. J Neurosci 1997;17:3751–65.

Killcross S, Robbins TW, Everitt BJ. Different types of fear-conditioned behaviour mediated by separate nuclei within amygdala. Nature 1997;388:377–80.

Kim SH, Chung JM. An experimental model for peripheral neuropathy produced by segmental spinal nerve ligation in the rat. Pain 1992;50:355–63.

LaLumiere RT, McGaugh JL. Memory enhancement induced by post-training intrabasolateral amygdala infusions of β-adrenergic or muscarinic agonists requires activation of dopamine receptors: involvement of right, but not left, basolateral amygdala. Learn Mem 2005;12:527–32.

LeDoux JE. Emotion circuits in the brain. Annu Rev Neurosci 2000;23:155–84.

Maren S. Synaptic mechanisms of associative memory in the amygdala. Neuron 2005;47:783–6.

McKernan MG, Shinnick-Gallagher P. Fear conditioning induces a lasting potentiation of synaptic currents in vitro. Nature 1997;390:607–11.

McWilliams LA, Cox BJ, Enns MW. Mood and anxiety disorders associated with chronic pain: an examination in a nationally representative sample. Pain 2003;106:127–33.

Nayak A, Zastrow DJ, Lickteig R, Zahniser NR, Browning MD. Maintenance of late-phase LTP is accompanied by PKA-dependent increase in AMPA receptor synthesis. Nature 1998;394:680–3.

Neugebauer V, Li W, Bird GC, Bhave G, Gereau RWt. Synaptic plasticity in the amygdala in a model of arthritic pain: differential roles of metabotropic glutamate receptors 1 and 5. J Neurosci 2003;23:52–63.

Neugebauer V, Li W, Bird GC, Han JS. The amygdala and persistent pain. Neuroscientist 2004;10:221–34.

Pare D, Quirk GJ, Ledoux JE. New vistas on amygdala networks in conditioned fear. J Neurophysiol 2004;92:1–9.

Parkinson JA, Willoughby PJ, Robbins TW, Everitt BJ. Disconnection of the anterior cingulate cortex and nucleus accumbens core impairs Pavlovian approach behavior: further evidence for limbic cortical-ventral striatopallidal systems. Behav Neurosci 2000;114:42–63.

Phelps EA, LeDoux JE. Contributions of the amygdala to emotion processing: from animal models to human behavior. Neuron. 2005;48:175–87.

Price DD. Central neural mechanisms that interrelate sensory and affective dimensions of pain. Mol Interv 2002;2:392–403, 339.

Rhudy JL, Meagher MW. Negative affect: effects on an evaluative measure of human pain. Pain 2003;104:617–26.

Russo CM, Brose WG. Chronic pain. Annu Rev Med 1998;49:123–33.

Sah P, Faber ES, Lopez DeArmentia M, Power J. The amygdaloid complex: anatomy and physiolog. Physiol Rev 2003;83:803–34.

Scholz J, Woolf CJ. Can we conquer pain? Nat Neurosci 2002;5(Suppl.):1062–7.

Scicli AP, Petrovich GD, Swanson LW, Thompson RF. Contextual fear conditioning is associated with lateralized expression of the immediate early gene c-fos in the central and basolateral amygdala nuclei. Behav Neurosci 2004;118:5–14.

Shi C, Davis M. Pain pathways involved in fear conditioning measured with fear-potentiated startle: lesion studies. J Neurosci 1999;19:420–30.

Shigetomi E, Kato F. Action potential-independent release of glutamate by Ca^{2+} entry through presynaptic P2X receptors elicits postsynaptic firing in the brainstem autonomic network. J Neurosci 2004;24:3125–35.

Soderling TR, Derkach VA. Postsynaptic protein phosphorylation and LTP. Trends Neurosci 2000;23:75–80.

Tanimoto S, Nakagawa T, Yamauchi Y, Minami M, Satoh M. Differential contributions of the basolateral and central nuclei of the amygdala in the negative affective component of chemical somatic and visceral pains in rats. Eur J Neurosci 2003;18:2343–50.

Tsuda M, Shigemoto-Mogami Y, Koizumi S, Mizokoshi A, Kohsaka S, Salter MW, et al. P2X4 receptors induced in spinal microglia gate tactile allodynia after nerve injury. Nature 2003;424:778–83.

Woolf CJ, Mannion RJ. Neuropathic pain: aetiology, symptoms, mechanisms, and management. Lancet 1999;353:1959–64.

Woolf CJ, Shortland P, Coggeshall RE. Peripheral nerve injury triggers central sprouting of myelinated afferents. Nature 1992;355:75–8.

Yu S, Undem BJ, Kollarik M. Vagal afferent nerves with nociceptive properties in guinea-pig oesophagus. J Physiol 2005;563:831–42.

Zald DH. The human amygdala and the emotional evaluation of sensory stimuli. Brain Res Brain Res Rev 2003;41:88–123.

Zimmermann M. Ethical guidelines for investigations of experimental pain in conscious animals. Pain 1983;16:109–10.

GLIA 55:604–616 (2007)

Involvement of $P2X_4$ and $P2Y_{12}$ Receptors in ATP-Induced Microglial Chemotaxis

KEIKO OHSAWA,[1] YASUHIRO IRINO,[1] YASUKO NAKAMURA,[1] CHIHIRO AKAZAWA,[1] KAZUHIDE INOUE,[2] AND SHINICHI KOHSAKA[1]*

[1]*Department of Neurochemistry, National Institute of Neuroscience, Kodaira, Tokyo 187-8502, Japan*
[2]*Department of Pharmacology, Graduate School of Pharmaceutical Sciences, Kyushu University, Higashi, Fukuoka 812-8582, Japan*

KEY WORDS
microglia; ATP; chemotaxis; P2Y12; P2X4

ABSTRACT
We previously reported that extracellular ATP induces membrane ruffling and chemotaxis of microglia and suggested that their induction is mediated by the Gi/o-protein coupled $P2Y_{12}$ receptor ($P2Y_{12}R$). Here we report discovering that the $P2X_4$ receptor ($P2X_4R$) is also involved in ATP-induced microglial chemotaxis. To understand the intracellular signaling pathway downstream of $P2Y_{12}R$ that underlies microglial chemotaxis, we examined the effect of two phosphatidylinositol 3′-kinase (PI3K) inhibitors, wortmannin, and LY294002, on chemotaxis in a Dunn chemotaxis chamber. The PI3K inhibitors significantly suppressed chemotaxis without affecting ATP-induced membrane ruffling. ATP stimulation increased Akt phosphorylation in the microglia, and the increase was reduced by the PI3K inhibitors and a $P2Y_{12}R$ antagonist. These results indicate that $P2Y_{12}R$-mediated activation of the PI3K pathway is required for microglial chemotaxis in response to ATP. We also found that the Akt phosphorylation was reduced when extracellular calcium was chelated, suggesting that ionotropic P2X receptors are involved in microglial chemotaxis by affecting the PI3K pathway. We therefore tested the effect of various $P2X_4R$ antagonists on the chemotaxis, and the results showed that pharmacological blockade of $P2X_4R$ significantly inhibited it. Knockdown of the $P2X_4$ receptor in microglia by RNA interference through the lentivirus vector system also suppressed the microglial chemotaxis. These results indicate that $P2X_4R$ as well as $P2Y_{12}R$ is involved in ATP-induced microglial chemotaxis.

INTRODUCTION

Microglia are the immune effector cells that participate in tissue repair, amplification of inflammatory responses, and neuronal degeneration in the central nervous system (CNS) (Kreutzberg, 1996; Streit, 2002). They are present in the form of ramified cells under normal conditions, but in response to pathological stimuli microglia rapidly transform into a motile ameboid form and migrate toward lesion sites, where they secrete a variety of substances and clear cell debris (Moran and Graeber, 2004; Nakajima and Kohsaka, 2005; Stence et al., 2001). Thus, microglial migration plays a crucial role in the amelioration of a damaged CNS; however, the intracellular signals underlying microglial cell migration are poorly understood.

Extracellular ATP is known to play a role as a neurotransmitter or neuromodulator in the CNS (Illes and Alexandre Ribeiro, 2004), and it regulates various physiological functions of microglia (Inoue, 2002). ATP receptors are classified into two families: the ionotropic P2X receptor (P2XR) family and the GTP-binding (G-) protein coupled P2Y receptor (P2YR) family (Ralevic and Burnstock, 1998), and microglia have been reported to possess functional ATP receptors, including $P2X_4R$, $P2X_7R$, and $P2Y_{12}R$ (Cavaliere et al., 2003; James and Butt, 2002; Sasaki et al., 2003; Tsuda et al., 2003). Davalos et al. (2005) and Nimmerjahn et al. (2005) recently reported that processes of ramified microglia extended toward a confocal laser injury, where ATP is likely to be released by damaged tissue and surrounding astrocytes. These observations suggest that ATP is a primary molecule in the induction of the change in microglial morphology.

We have also previously reported that ATP-induced microglial membrane ruffling and chemotaxis are mediated by Gi/o-protein coupled $P2Y_{12}R$ (Honda et al., 2001; Sasaki et al., 2003); however, the intracellular signaling pathway downstream of $P2Y_{12}R$ following ATP stimulation is not fully understood. Several recent articles have revealed that $P2Y_{12}R$ stimulation results in activation of the phosphatidylinositol 3′-kinase (PI3K) pathway in some cells (Czajkowski et al., 2004; Soulet et al., 2004; Van Kolen and Slegers, 2004). Although PI3K is known to be a crucial enzyme in the regulation of chemotaxis by monocytes and macrophages (Procko and McColl, 2005; Ridley, 2001; Van Haastert and Devreotes, 2004), whether the PI3K pathway participates in ATP-induced microglial chemotaxis remained unclear.

This article contains supplementary material available via the Internet at http://www.interscience.wiley.com/jpages/0894-1491/suppmat

Grant sponsors: Japanese Ministry of Health, Labour, and Welfare; Japanese Ministry of Education, Culture, Sports, Science, and Technology.

*Correspondence to: Shinichi Kohsaka, Department of Neurochemistry, National Institute of Neuroscience, 4-1-1 Ogawahigashi, Kodaira, Tokyo 187-8502, Japan. E-mail: kohsaka@ncnp.go.jp

Received 7 August 2006; Accepted 26 December 2006

DOI 10.1002/glia.20489

Published online 13 February 2007 in Wiley InterScience (www.interscience.wiley.com).

In this study we demonstrated that activation of the PI3K pathway is required for ATP-induced microglial chemotaxis and found that the PI3K/Akt activation was suppressed when extracellular Ca^{2+} was chelated. ATP stimulates P2XRs in microglia and causes an increase in intracellular calcium concentration ($[Ca^{2+}]_i$) by inducing an extracellular Ca^{2+} influx (Inoue et al., 1998; Tsuda et al., 2003). Therefore, to clarify involvement of P2XRs in microglial chemotaxis we also examined the effect of antagonists and RNA interference (RNAi) with P2XRs on microglial chemotaxis, and the results demonstrated that P2X$_4$R is involved in ATP-induced chemotaxis.

MATERIALS AND METHODS

Isolation of Microglia

Microglia were obtained from primary cell cultures of neonatal Wistar rat cerebral cortex as described previously (Nakajima et al., 1992). In brief, mixed glial cultures were maintained for 12–23 days in DMEM (Invitrogen, Carlsbad, CA) with 10% fetal calf serum (FCS) (Irvine Scientific, Santa Ana, CA). Microglia were prepared as floating cells by gentle shaking and allowed to attach to appropriate dishes or glasses.

Membrane Ruffling

Microglia attached to glass coverslips were incubated for 4 h in DMEM without FCS and stimulated with 50 μM ATP (Yamasashyoyu, Chiba, Japan) for 5 min at 37°C. The cells were then fixed with 3.7% formaldehyde for 10 min, permeabilized for 5 min with PBS containing 0.1% Triton X-100, and stained for 1 h with 2 U/mL Texas Red-conjugated phalloidin (Invitrogen) diluted in PBS containing 1%BSA. The cells were mounted in PermaFluor (Thermo Fisher Scientific, Waltham, MA) and examined under a fluorescence microscope AX70 (Olympus, Tokyo, Japan). To quantify membrane ruffles, cells were stained with 1 μg/mL anti-Iba1 polyclonal antibody (Imai et al., 1996) and Alexa Fluor 488-conjugated anti-rabbit IgG (1:1,000, Invitrogen) and then incubated with 2 U/mL Alexa Fluor 647-conjugated phalloidin (Invitrogen). The F-actin content of cells positive for Iba1 was quantified as the integral intensity of Alexa Fluor 647 fluorescence with a laser scanning cytometer (LSC2, CompuCyte, Cambridge, MA). The mean fluorescent intensity of the cells pretreated with each inhibitor was calculated from the data obtained from 1,000 cells. Increases in membrane ruffles are reported as ratios of the mean fluorescent intensity of the ATP-stimulated cells to that of the unstimulated cells. The effect of the inhibitors was assessed by preincubating cells with wortmannin (Sigma, St. Louis, MO) (100 nM) for 20 min, LY294002 (Wako, Osaka Japan) (50 μM) for 20 min, AR-C69931MX (AstraZeneca, UK) (1 μM) for 10 min, 2′,3′-*O*-(2,4,6-trinitrophenyl) adenosine 5-triphosphate (TNP-ATP) (Invitrogen) (100 μM) for 5 min, pyridoxal-phosphate-6-azophenyl-2′,4′-disulfonic acid (PPADS) (Sigma) (300 μM) for 5 min, or Brilliant blue G (BBG) (Nacalai Tesque, Kyoto, Japan) (1 μM) for 5 min, and then stimulating them with ATP.

Chemotaxis Assay

Dunn chemotaxis chambers (Weber Scientific International, Teddington, UK) were used to perform the chemotaxis assays according to the method described previously (Honda et al., 2001; Webb et al., 1996). In brief, microglia attached to square coverslips were incubated for 4 h in DMEM without FCS. Each coverslip was then inverted onto a chamber and the medium in the outer well was replaced with DMEM containing 50 μM ATP. The chamber was placed on the stage of a microscope (ECLIPSE TE300; Nikon, Tokyo Japan), and cell images were collected every 5 min for 1 h with a CCD camera (Hamamatsu Photonics, Hamamatsu, Japan) and imaging software (fishPPC; Hamamatsu Photonics). Time-lapse video images were used to calculate the final position of cells relative to their starting position, and the distance each cell migrated was measured by plotting the positions of the cell nucleus on a computer display with software (Image-Pro Plus; Media Cybernetics, MD). The distance and direction moved are shown as x and y coordinates on scatter diagrams in which the x-axis is parallel to the outer ring and the position of the outer well is above the y-axis.

Akt Activation

Microglia were incubated for 4 h in DMEM without FCS and then stimulated with 50 μM ATP or 100 ng/mL recombinant murine macrophage-colony stimulating factor (M-CSF) (R&D Systems, Minneapolis, MN) for 5 min at 37°C, and lysed with SDS sample buffer. Proteins were separated by 10% SDS-PAGE and transferred onto an Immobilon P membrane (Millipore, MA). The membrane was incubated for 1 h at room temperature with a blocking solution containing 25 mM Tris, pH 7.5, 150 mM NaCl, 0.1%(v/v) Tween 20 (TTBS), and 5% (v/v) nonfat dry milk, and then incubated overnight at 4°C with mouse monoclonal anti-phospho-Akt (Ser473) antibody (diluted 1:1,000, Cell Signaling Technology, Beverly, MA) or rabbit polyclonal Akt antibody (diluted 1:1,000, Cell Signaling Technology). The membrane was incubated for 1 h at room temperature with horseradish peroxidase (HRP)-conjugated donkey anti-mouse IgG (diluted 1:1,000, GE Healthcare, Little Chalfont, UK) or HRP-conjugated donkey anti-rabbit IgG (diluted 1:1,000, GE Healthcare), and phosphorylated Akt and total Akt were detected with an ECL Western blotting detection system (GE Healthcare). The Akt phosphorylation level was quantified by densitometry with NIH image software. Before stimulating the cells in the calcium-depleted experiment, they were incubated for 30 min in a balanced salt solution composed of 20 mM Hepes, pH7.4, 150 mM NaCl, 5 mM KCl, 1.2 mM $MgCl_2$, and 10 mM glucose in the presence of 1.2 mM Ca^{2+} (BSS) or 1 mM ethy-

lene glycol-*bis*(2-aminoethyl)-*N,N,N,N*-tetraacetic acid (EGTA) (Ca^{2+}-free BSS).

Construction of Lentivirus Vectors Expressing Interfering Short Hairpin RNA (shRNAi) and Microglial Transduction

Lentivirus containing shRNAi was prepared by the method previously described (Yogosawa et al., 2005). The self-inactivating (SIN) vector construct pCS-RfA-CG, which contains the EGFP gene under the control of the CMV promoter and sites for site-specific recombination with a Gateway vector (attR1,2), was used for simultaneous expression of EGFP and shRNA. Plasmid containing $P2X_4R$ shRNAi under the control of human U6 promoter was provided by Dr. K. Inoue (Kyushu Univ. Fukuoka, Japan). The gene of the $P2X_4R$ shRNAi-expressing cassette inserted into pENTR™1A was transferred into the pCS-RfA-CG by a recombination reaction using Gateway LR Clonase (Invitrogen). The sequence of shRNA targeted for firefly luciferase was used as a control (Nishitsuji et al., 2004). The sequence was inserted into the piGENE™ hU6 *Bsp*MI vector (iGENE Therapeutics, Tsukuba, Japan), and the gene of the luciferase shRNAi-expressing cassette was ligated into the pCS-RfA-CG. The sequence of $shP2X_4R$ was: 5′-GGG ATA AGA GAT ATA GGT AAC GTG TGC TGT CCG TTA CTT ATA TTT CTT GTC CCT TTT T-3′. We confirmed the specificity of P2×4R shRNAi by a coexpression assay. pCS-shP2×4R-CG was cotransfected into Cos7 cells with P2×4 expression plasmid (provided by Dr. K. Inoue) or HA-tagged P2Y12R plasmid (Supplemental information). pCS-shP2×4R-CG significantly suppressed P2×4R expression but had no effect P2Y12R expression. The recombined plasmid was cotransfected into 293FT cells (Invitrogen) with a packaging plasmid (pCAG-HIVgp) and a plasmid expressing Rev and vesicular stomatitis virus G glycoprotein (pCMV-VSV-G-RSV-Rev), and the supernatant was collected after 48 h and filtered through a 0.45-μm pore filter (Falcon). Viral particles in the supernatant were concentrated by ultracentrifugation for 2 h at 19,400 rpm (SW28 rotor; Beckmann Coulter, CA) and recovered by suspension in Hanks buffered saline (Invitrogen).

The recombinant lentivirus (2×10^5 infectious units) was added to the mixed glial cells that had been cultured for 12 days in a 25-cm^2 flask, and cultured for 6 days in DMEM containing 10% FCS. Floating cells were collected as microglia and allowed to attach to appropriate dishes or glasses. The efficiency of microglia transduction with the $shP2X_4R$ vector was 20–30%, the same as with the shControl vector according to an analysis of the number of microglia expressing EGFP by flow cytometry.

Isolation of EGFP-Positive Microglia

After transduction with the lentivirus vectors, floating cells collected as microglia were resuspended in PBS containing 2% FCS. EGFP-positive and -negative cells were sorted with a FACSVantageSE flow cytometry system (BD Biosciences). Live gating was performed with propidium iodide (Sigma-Aldrich, St. Louis, MO). The purity of the EGFP-positive cells was >99% according to a flow cytometry analysis.

Western Blot Analysis of P2X Receptor Expression

Sorted cells were lysed in SDS sample buffer. $P2X_4R$, $P2X_7R$, EGFP, and actin proteins in the lysate equivalent to 2×10^4 cells were separated by 10% SDS-PAGE and detected by Western blot analysis with 1 μg/mL anti-$P2X_4R$ antibody (Alomone Labs, Jerusalem, Israel), 0.6 μg/mL anti-$P2X_7R$ (Alomone Labs), anti-GFP antibody (diluted 1:1,000, Medical & Biological Laboratories, Nagoya, Japan), and anti-actin antibody (diluted 1:1,000, Sigma), respectively, and visualized with the ECL system.

RT-PCR Analysis for $P2Y_{12}R$ Gene Transcripts

RNA was isolated from the sorted cells with the RNeasy Mini Kit (QIAGEN, Hildem, Germany) containing a DNase treatment, according to the manufacturer's protocols. Reverse transcription of RNA was performed with SuperScript III reverse transcriptase (Invitrogen). The PCR amplification conditions were 30 s at 94°C, 15 s at 60°C, and 30 s at 68°C for 25–35 cycles, except for the initial denaturation step of 2 min at 94°C and the final cycle with an elongation step of 5 min at 68°C. An extra reaction mixture without reverse transcriptase was used as a control for DNA contamination of the RNA sample. The primers used were as follows: rat $P2Y_{12}R$, 5′-AAA CTT CCA GCC CCA GCA ATC T-3′ (forward), 5′-CAA GGC AGG CGT TCA AGG AC-3′ (reverse); rat β-actin, as an internal standard, 5′-TTG TTA CCA ACT GGG ACG ACA TGG-3′ (forward), 5′-GAT CTT GAT CTT CAT GGT GCT AGG-3′ (reverse). PCR products of 447 bp for $P2Y_{12}R$ and 763 bp for β-actin were analyzed on a 1.5% agarose and stained with ethidium bromide. The relative intensity of the bands for $P2Y_{12}R$ was quantified by densitometry with NIH image software and normalized to the β-actin products. The normalized values were used to calculate the ratio of $P2Y_{12}R$ mRNA level in the EGFP-positive cells transduced with the $shP2X_4R$ vector to the level in the EGFP-positive cells transduced with the shControl vector.

Calcium Imaging

The intracellular calcium concentration ($[Ca^{2+}]_i$) was monitored by the fura-2 method described by Inoue et al. (1998), using a highly sensitive intensifier target video camera C2400 and an Argus 50 image processor (Hama-

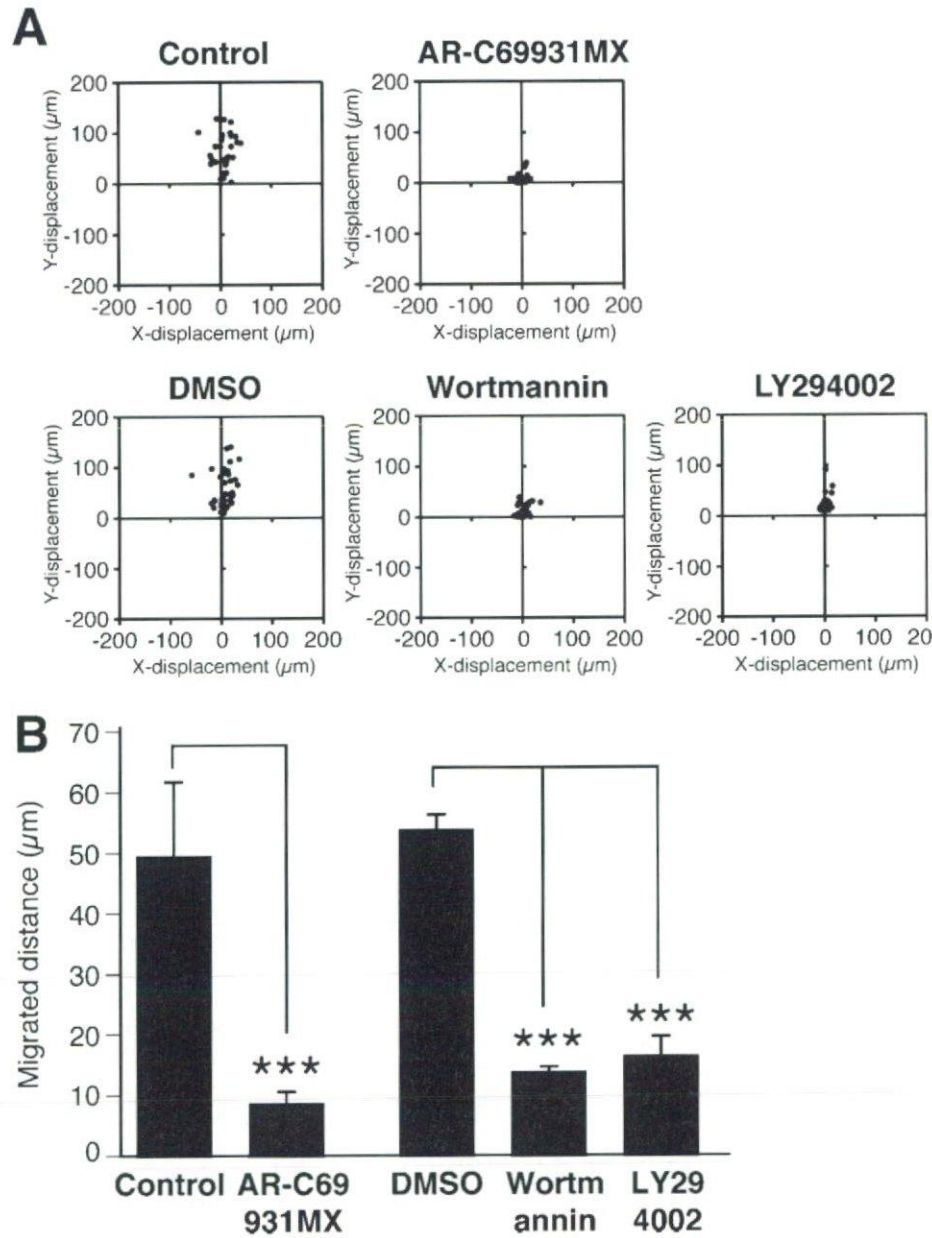

Fig. 1. Effect of PI3K inhibitors on ATP-induced microglial chemotaxis. (**A**) Microglia were pretreated with 1 μM AR-C69931MX for 10 min or with 0.125% DMSO, 100 nM wortmannin, or 50 μM LY294002 for 20 min, and microglial migration towards 50 μM ATP was observed in the Dunn chemotaxis chamber. The distance and direction migrated by individual cells are shown as x and y coordinates on scatter diagrams. The position of the outer well of the chamber is at the top in the vector diagrams of cells. (**B**) Chemotaxis by each cell was quantified by measuring the (x, y) distance migrated from the starting position. Data are means ± SD of three independent experiments. $^{***}P < 0.001$, Student's t-test.

matsu Photonics). Microglia transduced with the lentivirus vectors were plated at 2×10^5 cells/well on poly-L-lysine-coated CELLocate microgrid coverslips (Eppendorf, Hambrug, Germany). After 2 h, the cells were incubated with 10 μM fura-2 acetoxymethylester (fura-2/AM, Dojindo Laboratories, Kumamoto, Japan) at 37°C for 30 min in DMEM containing 25 mM HEPES (DMEM-H, Invitrogen), and the coverslips were mounted on an inverted epifluorescence microscope (TMD-300, Nikon, Tokyo, Japan). The cells were exposed to drugs dissolved in DMEM-H by superfusion. Raw data were recorded as 500-nm emissions of fura-2 excited alternately at 340 and 380 nm, and $[Ca^{2+}]_i$ was expressed as the ratio of the fluorescence intensity at 340 nm to the fluorescence intensity at 380 nm (F340/380).

RESULTS

Involvement of the PI3K Pathway in ATP-Induced Microglial Chemotaxis

We previously reported that ATP-induced microglial membrane ruffling were inhibited by treatment with pertussis toxin and a P2Y$_{12}$R-selective antagonist, AR-C69931MX, suggesting that Gi/o-coupled P2Y$_{12}$R is involved in both the membrane ruffling and the chemotaxis (Honda et al., 2001). Stimulation of P2Y$_{12}$R has been reported to induce PI3K activation (Czajkowski et al., 2004; Soulet et al., 2004; Van Kolen and Slegers, 2004). To determine whether PI3K activation is required for chemotaxis by ATP-stimulated microglia, we investigated the effects of the PI3K inhibitors wortmannin and

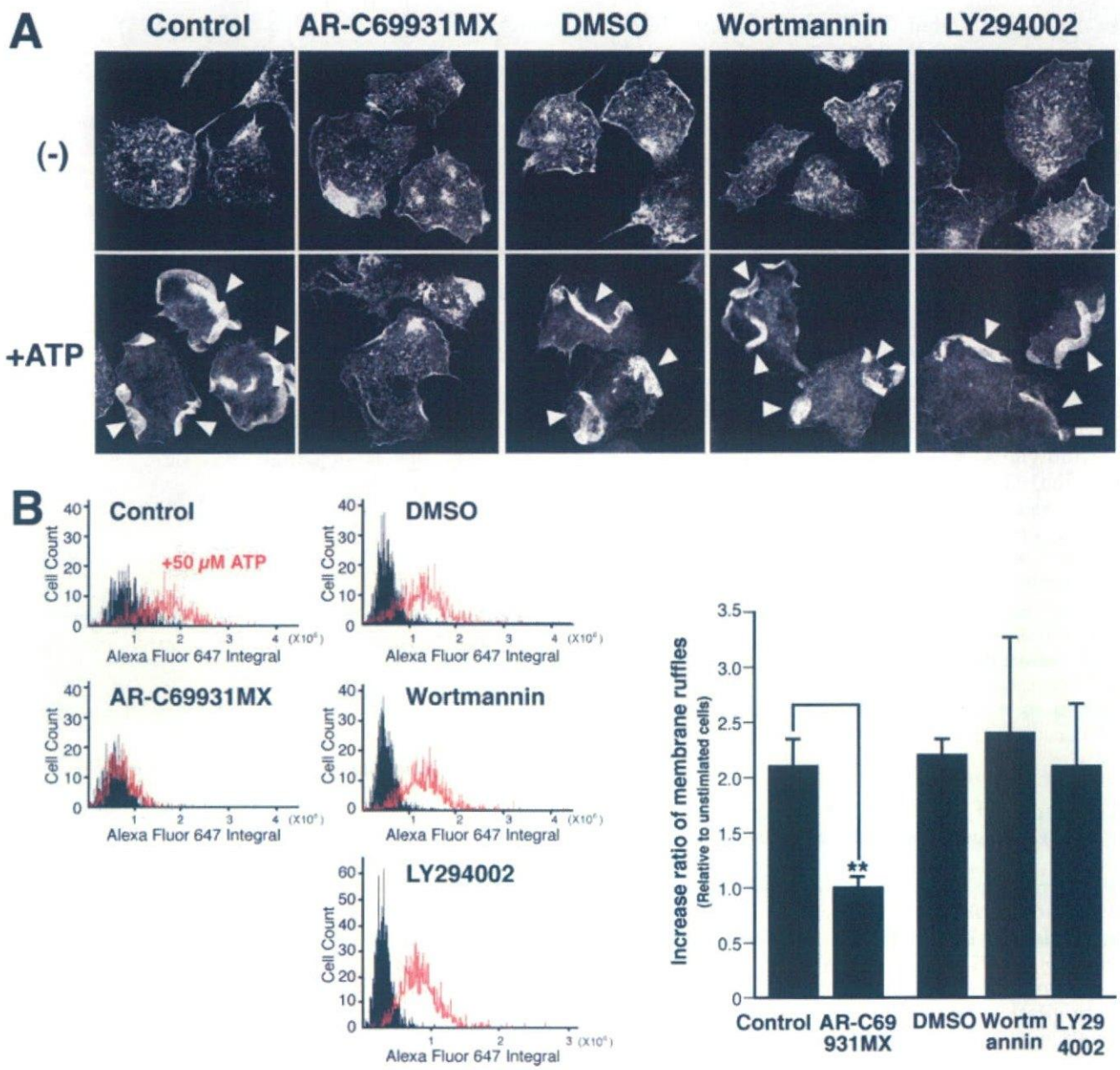

Fig. 2. Effect of PI3K inhibitors on ATP-induced microglial membrane ruffling. (**A**) Microglia were pretreated with 1 μM AR-C69931MX, 0.125% DMSO, 100 nM wortmannin, or 50 μM LY294002 as described in Fig. 1A, and then stimulated with 50 μM ATP for 5 min. After fixation, the cells were stained with Texas Red-conjugated phalloidin to visualize membrane ruffles. Arrowheads indicate membrane ruffles. Scale bar, 10 μm. (**B**) Quantification of membrane ruffles. Microglia were stimulated as in A for 5 min, fixed, and stained with an anti-Iba1 antibody and Alexa Fluor 647-conjugated phalloidin to recognize individual microglial cells and membrane ruffles, respectively. The F-actin content of microglial cells was quantified as integral intensity of Alexa Fluor 647 fluorescence by using LSC. The five panels on the left side are histograms representing the total F-actin in each cell (*x*-axis, Alexa fluor 647 integral) and the number of scanned cells (*y*-axis, cell count). The black region represents the unstimulated cells, and the region surrounded by the red line represents the ATP-stimulated cells. The bar graph on the right side shows the ratio of the mean of fluorescent intensity of ATP-stimulated cells to that of unstimulated cells after treatment with each inhibitor. Data are means ± SD of three independent experiments. $^{**}P < 0.01$, Student's *t*-test.

LY294002 with a Dunn chemotaxis chamber. Microglial chemotaxis toward the higher concentration of ATP was evaluated by analysis of time-lapse images. When 50 μM ATP was applied to the outer well, the cells migrated toward higher concentrations of ATP. Pretreatment of the microglia with wortmannin or LY294002 significantly blocked the chemotaxis (Fig. 1A). The chemotactic movement of the microglia was quantified by calculating the (x, y) distances individual cells migrated toward ATP. As shown in Fig. 1B, the mean distance migrated by cells pretreated with PI3K inhibitors was significantly shorter than the distance migrated by cells pretreated with DMSO. Treatment with 1 μM AR-C69931MX also inhibited the chemotaxis, as expected based on the results of our previous study (Honda et al., 2001). These findings suggested that PI3K activation is necessary for ATP-induced microglial chemotaxis.